NJC

ROYAL SOCIETY OF CHEMISTRY

PAPER

View Article Online
View Journal | View Issue

Cite this: *New J. Chem.*, 2024, **48**, 7761

Antioxidant, hemostatic, and injectable hydrogels with photothermal antibacterial activity to accelerate full-thickness wound regeneration†

Vajihe Alinezhad,[a] Reza Ghodsi,[b] Hadi Bagheri,[c] Farzaneh Mahmoudi Beram,[d] Habib Zeighami,[e] Ali Kalantari-Hesari,[f] Laleh Salarilak,[a] Ebrahim Mostafavi,[gh] Zainab Ahmadian,[i] Mohammad-Ali Shahbazi*[j] and Aziz Maleki *[ab]

Developing injectable hydrogel dressings with multifunctional properties, including antibacterial and antioxidant ability, and good mechanical properties to treat infected full-thickness skin wounds is of particular importance in clinical applications. The incorporation of metal ions, such as Zn^{2+}, Ca^{2+}, and Fe^{2+}, confers the hydrogels with unique properties, including conductivity, bioactivity, and tunability. In this study, a multifunctional near-infrared (NIR) active hydrogel, named Alg–HA–Zn–PDA, was fabricated *via* the incorporation of polydopamine (PDA) nanoparticles into hyaluronic acid (HA) and alginate (Alg) crosslinked by Zn^{2+}. This hydrogel exhibited high porosity, good mechanical properties, and high water content, which is an essential requirement in the adsorption of exudates during the healing process. PDA endowed the hydrogels with antioxidant activity and hemostatic ability, and made the hydrogels NIR active. Zn^{2+} could contribute to the antibacterial and healing effects of the hydrogels. The antibacterial activity of Alg–HA–Zn–PDA, with and without NIR irradiation against *Escherichia coli* (*E. coli*) and *Staphylococcus aureus* (*S. aureus*), showed that the NIR light irradiation could result in heat generation and destroy the bacteria. Furthermore, *in vivo* treatment in a *S. aureus*-infected full-thickness skin defect model demonstrated that the Alg–HA–Zn–PDA hydrogel possesses excellent wound closure capacity in the presence of NIR irradiation. In summary, we concluded that the developed antibacterial, hemostatic, and antioxidant hydrogel is an excellent candidate for wound dressing for the repair of full-thickness skin defects.

Received 21st December 2023,
Accepted 21st March 2024

DOI: 10.1039/d3nj05871a

rsc.li/njc

1. Introduction

One-third of the global mortality is related to bacterial infectious diseases, causing tremendous harm to human health.[1] The skin plays a vital protective role in protecting the body from external harm; thus, it is of special importance to accelerate the treatment of damaged skin tissues, especially bacterial infected ones.[2] Benefiting from their favorable biocompatibility, distinctive physicochemical properties, and ability to simulate the natural extracellular matrix, hydrogels are often used as excellent wound dressings. They have a three-dimensional and porous structure and can absorb a large quantity of water, thus providing a moist environment to the wound environment.[3–5] Due to wounds on the skin being often irregular in shape, conventional hydrogels cannot cover the wounds. Therefore, injectable counterparts have recently gained great attention because of their potential for filling an irregular wound.[6–8] Hyaluronic acid (HA) is a biocompatible, biodegradable, and non-toxic natural polymer with gelation properties, and has been extensively used in the construction of injectable dressings.

[a] *Department of Pharmaceutical Nanotechnology, School of Pharmacy, Zanjan University of Medical Sciences, 45139-56184 Zanjan, Iran. E-mail: Maleki@zums.ac.ir*
[b] *Zanjan Pharmaceutical Nanotechnology Research Center (ZPNRC), Zanjan, Iran*
[c] *Student Research Committee, School of Pharmacy, Zanjan University of Medical Sciences, Zanjan, Iran*
[d] *Department of Chemistry, Faculty of Chemistry, Isfahan University, Isfahan, Iran*
[e] *Department of Microbiology, School of Medicine, Zanjan University of Medical Sciences, Zanjan, Iran*
[f] *Department of Pathobiology, Faculty of Veterinary Medicine, Bu-Ali Sina University, Hamedan, Iran*
[g] *Stanford Cardiovascular Institute, Stanford University School of Medicine, Stanford, CA, 94305, USA*
[h] *Department of Medicine, Stanford University School of Medicine, Stanford, CA, 94305, USA*
[i] *Department of Pharmaceutics, School of Pharmacy, Lorestan University of Medical Sciences, Khorramabad, Iran*
[j] *Department of Biomaterials and Biomedical Technology, University Medical Center Groningen, University of Groningen, Antonius Deusinglaan 1, Groningen 9713 AV, The Netherlands. E-mail: m.a.shahbazi@umcg.nl*

† Electronic supplementary information (ESI) available. See DOI: https://doi.org/10.1039/d3nj05871a

It can stimulate cell migration, mediate cellular signaling, reduce inflammation, and promote angiogenesis to accelerate the repair process of an injured wound.[9–12] Alg is a naturally occurring polysaccharide derived from brown algae. It can form viscous, hydrophilic, and biocompatible hydrogels when it is hydrated.[13] In addition, it can be electrochemically cross-linked with metal cations to form multifunctional hydrogels.[14,15] Due to its low toxicity, biocompatibility, and similarity to the extracellular matrix (ECM), it is widely used in the design and fabrication of hydrogels, especially in wound healing applications.[16,17] Although Alg and HA have been broadly used in the fabrication of hydrogels, the polymers alone cannot address all the requisite properties for a successful wound dressing.[18–20] Therefore, their combination with other polymers, NPs, or biologically active metal ions can boost the performance of the polymers in the wound repair process.[21,22] This is due to the fact that wound healing is a complex process involving multiple phases *i.e.*, hemostasis, inflammation, proliferation, and remodeling.[23] In addition, PDA with excellent biocompatibility, water dispersity, effective radical scavenging ability, and strong tissue adhesion, has drawn increasing attention in broad biomedical applications, especially in the preparation of multifunctional wound dressings.[24,25] It has excellent photothermal conversion efficiency, making it a good candidate for photothermal therapy (PTT).[26] Also, PDA has highly reactive catechol functional groups, the key component of mussel adhesive proteins for adhering to many surfaces in aqueous environments, rendering it of merit to be used in the fabrication of adhesive hydrogels with self-healable properties.[27,28] However, the majority of the existing PDA-based hydrogels require complex modification or synthesis, which might hinder them from further application.[29–31] Therefore, it is imperative to develop PDA-based injectable hydrogels through facile preparation.[32]

The metal–ligand coordination interaction with a capacity to produce hydrogels with high mechanical properties has attracted increasing attention to preparing advanced hydrogels for wound healing management.[33] Many metal ions have shown crucial roles in tissue regeneration.[34,35] Therefore, the incorporation of metal ions into hydrogels can expand/improve the performance of the porous materials.[36–38] Among the ions, Zn^{2+} is a component structure of enzymes maintaining the structural integrity of proteins and regulating gene expression.[39] In the wound healing process, the ions reduce free radical activity, accelerate collagen synthesis and cellular growth, and inhibit bacterial growth.[40,41] However, Zn-based adhesive hydrogels have been rarely reported as a wound sealant.[41] Collectively, as far as we know, no studies on the fabrication and characterization of injectable hydrogels prepared from Alg, HA, PDA, and zinc ions have been carried out.[42–44]

Herein, taking advantage of the unique properties of HA, Alg, and PDA, an antibacterial, antioxidant, and hemostatic hydrogel was constructed by the use of Zn^{2+} as a crosslinker (named Alg–HA–Zn–PDA; Fig. 1). The multifunctional hydrogels exhibited proper rheological properties and excellent photothermal behavior *in vitro*. The antibacterial, hemostatic ability and antioxidant activity of the hydrogels were investigated. Good hemocompatibility and cytocompatibility were also demonstrated to prove the biocompatibility of the hydrogels. In addition, the NIR-active hydrogels exhibited excellent antibacterial capability against *S. aureus* and *E. coli in vitro*. This property was further increased when NIR light (808 nm) was used. The enhanced effect of the photothermally active hydrogels on accelerating wound healing using a rat full-thickness wound defect model was studied in terms of wound closure and histomorphological examinations. In summary, all of the achievements demonstrated the excellent potential of the antibacterial and hemostatic hydrogels with appropriate mechanical properties, photothermal effect, antioxidant activity, and biocompatibility for wound healing applications.

2. Materials and methods

2.1. Materials

Dopamine hydrochloride, sodium alginate, hyaluronic acid, 1,1-diphenyl-2-picryl-hydrazyl (DPPH), Dulbecco's modified Eagle's medium (DMEM), Zn $(NO_3)2{\cdot}6H_2O$, fetal bovine serum (FBS), penicillin/streptomycin, and 3-[4,5-dimethylthiazol-2-yl]-2,5-diphenyltetrazolium bromide (MTT) were purchased from Sigma-Aldrich. *S. aureus* (ATCC25923) and *E. coli* (ATCC25922) were purchased from the Pasteur Institute of Iran. NIH_3T_3 cells were obtained from the Iranian Biological Resource Center (ATCC, CRL-1658).

2.2. Synthesis of PDA NPs

PDA NPs were synthesized according to the previously reported study.[45] Briefly, ammonia aqueous solution (1 mL, NH_4OH, 28–30%) was added into ethanol (20 mL) and deionized water (45 mL) under mild stirring at 30 °C for 30 min. Dopamine hydrochloride (0.25 g) dissolved in deionized water (5 mL) and then added into the above solution dropwise. The color of the resulting solution turned to pale yellow and gradually changed to dark brown. After 24 h reaction, the NPs were obtained by centrifugation, and washed with deionized water three times before dispersing in deionized water.

2.3. Preparation of the hydrogels

To prepare the hydrogel, 400 μL Alg (10% w/v) and 400 μL HA (1% w/v) were mixed to obtain a homogenous mixture. Then, 200 μL Zn^{2+} solution (0.1 M) was added to the previous mixture. The mixture was vortexed to obtain Alg–HA–Zn hydrogel. To prepare Alg–HA–Zn–PDA hydrogel, the same amounts of Alg and HA were mixed with PDA (5 mg mL^{-1}, 10 μL) to make a homogenous mixture and then the Zn^{2+} solution as a cross linker was added to construct Alg–HA–Zn–PDA hydrogel.

2.4. Characterization of PDA NPs and the hydrogels

The morphology and microstructure of the PDA NPs and the hydrogels were evaluated by scanning electron microscopy (SEM, Quanta 250 FEG, USA). The surface functional groups of the hydrogels were confirmed by Fourier transform infrared

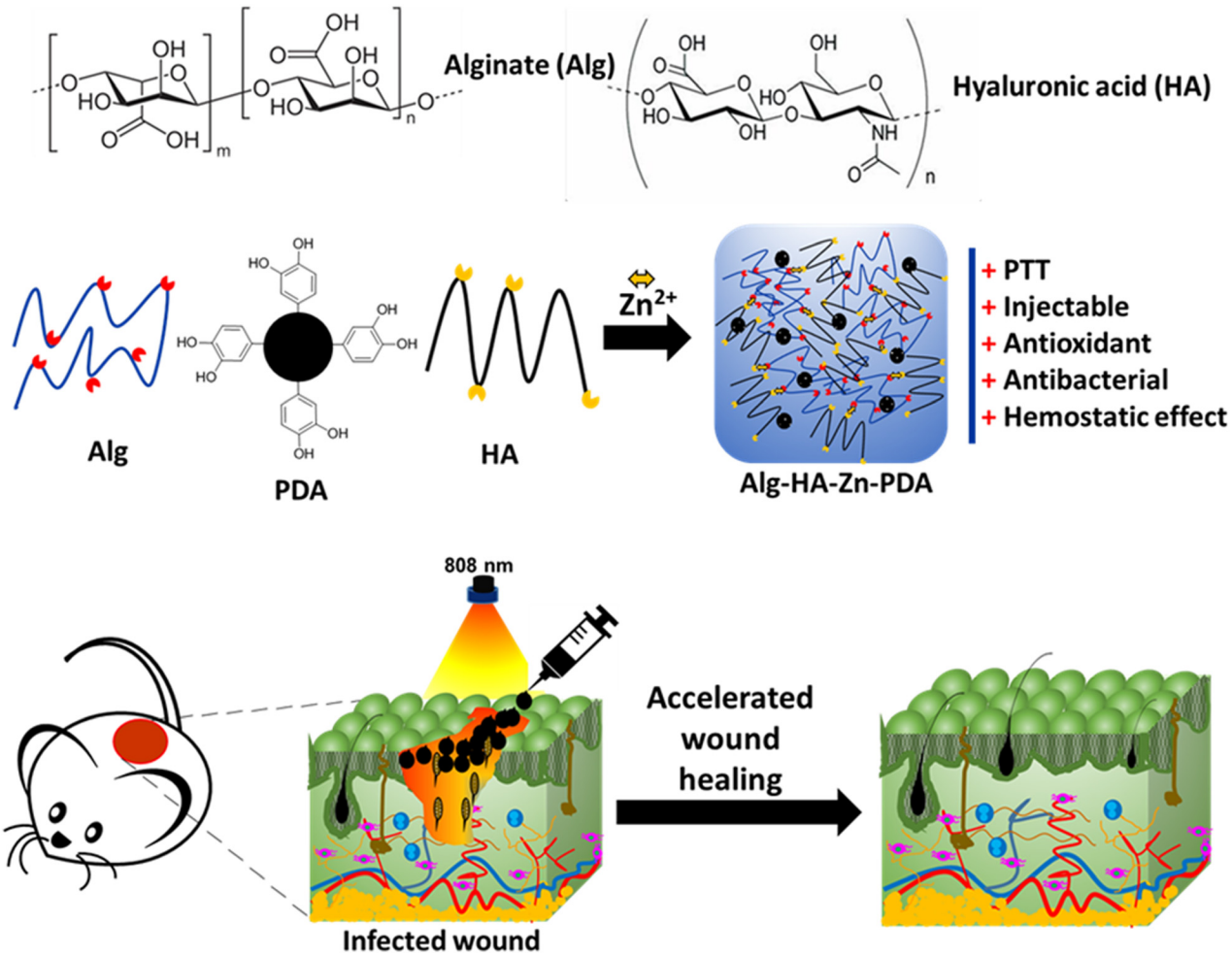

Fig. 1 Schematic illustration of Alg–HA–Zn–PDA hydrogel preparation with NIR irradiation to promote wound healing. PDA: polydopamine, PTT: photothermal therapy.

spectroscopy (FTIR, Bruker, Tensor 27, Germany) in the wavenumber region of 4000–400 cm^{-1}. The crystallinity of all samples was carried out by X-ray diffraction (XRD, PW 1730, Philips, Netherlands) in the 2θ range of 10°–80°. The pyrolysis behaviors of all samples were investigated by thermogravimetric analysis (TGA, SDT-Q600, USA). The UV-vis-NIR analysis of the PDA NPs, Alg–Zn, and Alg–HA–Zn hydrogels were studied by a UV-vis spectrophotometer (Bruker IFS, 66/vs). Analysis of the hydrogel's elements was performed by energy dispersive spectroscopy (EDS, TESCAN, MIRAIII, Czech Republic). To measure the zeta potential of the PDA NPs, dynamic light scattering (DLS) (Malvern, UK) was used.

2.5. The rheology property of the hydrogels

The rheological performance of the hydrogels was conducted by a TA rheometer (MCR300, Anton Paar, USA). Storage modulus (G') and loss modulus (G'') were obtained by frequency sweep test (0.01–100 Hz). The shear thinning property of the hydrogels was carried out by parallel plate geometry (75 mm diameter) with a 300 S interval at room temperature using a rheometer (R/S Brookfield, Canada).

2.6. Swelling and degradation

The freeze-dried hydrogels were allowed to hydrate in excess PBS solution (pH ~7.4) at room temperature. The hydrating samples were weighed at timed intervals after excess water was removed by filter paper. The swelling percentage is defined as:

$$\text{Swelling percentage\%} = S_1/S_0 \times 100 \quad (1)$$

where S_1 is the weight of the hydrogel at different times and S_0 is the initial weight of the hydrogel at time 0 h. Three samples were tested for each time.

The *in vitro* degradation of the hydrogels was examined as a function of weight loss under aqueous conditions in PBS (pH ~ 7.4). The freeze-dried hydrogels were weighed (W_0) and immersed in PBS solution. After a predetermined time, the residual hydrogels were removed from the solution, and then freeze-dried and weighed (W_t). The degradation was assessed by measuring the weight remaining (%), which is defined as the following equation:

$$\text{Weight remaining\%} = W_t/W_0 \times 100 \quad (2)$$

where W_0 and W_t are the weights of the freeze-dried hydrogels before and after degradation, respectively. Three samples were tested for each time.[46,47]

2.7. Zinc ion release

To evaluate the Zn ion release from the Alg–HA–Zn–PDA hydrogel, the samples were immersed in 20 mL of PBS using a dialysis bag and incubated at 37 °C. At time intervals of 15 min, 30 min, 1 h, 2 h, 4 h, 6 h, 12 h, and 24 h, 7 mL of the released medium was taken and replaced immediately with fresh PBS in the same volume. The taken samples were used to measure Zn ion release by atomic absorption spectroscopy using an atomic absorption spectrometer (Spectra 110-Varian).[48]

2.8. Photothermal performance of PDA NPs and Alg–HA–Zn–PDA hydrogel

The photothermal activity of the PDA NPs (1 mL aqueous solution) and Alg–HA–Zn–PDA hydrogel (1 mL) with different concentrations (method 2.3.) was investigated under 808 nm NIR laser at power densities of 0.5, 1, and 1.5 W cm^{-2} for 10 min. An infrared thermal camera (TiS55, Fluke, USA) was used to record the temperature every 1 minute. The photothermal stability of the Alg–HA–Zn–PDA hydrogel was explored by four cycles of laser on–off. The photothermal conversion efficiency (η) of the Alg–HA–Zn–PDA hydrogel was studied according to the previous method.[45,49,50] To this aim, 1 mL of the Alg–HA–Zn–PDA hydrogel was exposed under 808 nm (1 W cm^{-2}) for 10 min. Then, the temperature was recorded every 30 s in the cooling phase for 10 min. Detailed calculations were given as follows:

$$\eta = \frac{hS(T_{max} - T_{surr}) - Q_o}{I\left(1 - 10^{-A^{808}}\right)} \quad (3)$$

where h is the heat transfer coefficient, S is the surface area of the container, $T_{max} - T_{surr}$ represents the difference between the maximum temperature of the hydrogel after laser irradiation and the surrounding temperature, resulting in the η value, Q_o is the heat associated with the light absorbance of the solvent, and I refers to laser power density. A^{808} is the absorbance of the PDA NPs at the wavelength of 808 nm. The time constant heat transfer (τ_s) was measured by linear time data *versus* –Ln(θ) from the cooling phase, as follows:

$$\tau_s = \frac{t}{-\mathrm{Ln}(\theta)} \quad (4)$$

The θ value was measured using the equation:

$$\theta = \frac{T - T_{min}}{T_{max} - T_{min}} \quad (5)$$

where T refers to the temperature at each time point. Then, hS was measured by the following equation:

$$hS = \frac{m_i c_i}{\tau_s} \quad (6)$$

where m_i is the weight of the dried hydrogel, and c_i is the heat capacity of the solvent, which is 4.2 J g^{-1} k^{-1}. After that, deionized water (solvent) (1 mL) was exposed under an 808 nm laser for 10 min. Then, the temperature was determined in the cooling phase and all the above-mentioned processes were repeated for the solvent. Q_o is the heat associated with the light absorbance of the solvent per second. It was calculated by the following equation:

$$Q_o = hS(T_{max,water} - T_{surr}) \quad (7)$$

$T_{max,water} - T_{surr}$, was achieved between the maximum temperature of deionized water and the surrounding temperature.

2.9. Hemolysis effect

The hemocompatibility of the Alg–HA–Zn and Alg–HA–Zn–PDA hydrogels was studied by hemolysis assay using a human erythrocyte suspension *in vitro*.[51] To obtain fresh RBCs, whole anticoagulant blood was centrifuged at 3000 rpm for 6 min with PBS (pH ~7.4). The separated RBC was washed five times and diluted to 5% (v/v) by PBS. Then, different amounts of the hydrogels in 500 μL PBS buffer were mixed with the RBC suspension (100 μL) to obtain mixtures with different concentrations (1, 2, 3, and 4 mg mL^{-1}). After incubation for 2, 4, 8, and 24 h, the samples were centrifuged at 3,000 rpm for 6 min. The supernatants (150 μL) were transferred to a 96-well plate and the absorbance at 540 nm was calculated by a microplate reader. The hemolysis percentage was followed by:

$$\text{Hemolyzed RBCs}\,(\%) = \frac{(A_s - A_n)}{(A_p - A_n)} \times 100 \quad (8)$$

or

$$\text{Non-hemolyzed RBCs}\,(\%) = 1 - \frac{(A_s - A_n)}{(A_p - A_n)} \times 100 \quad (9)$$

where, A_s, A_n, and A_p were the absorbance of the hydrogel, PBS, and deionized water, respectively.

2.10. *In vitro* cytotoxicity of the hydrogels

An MTT assay was performed to study the cytocompatibility of the hydrogels. Mouse embryo fibroblast cells (NIH_3T_3) were seeded into a 96 well-plate (2×10^6 cell per mL) in each well with 200 μL of culture medium containing DMEM with 10% fetal bovine serum and 1% penicillin–streptomycin solution in a CO_2 incubator at 37 °C. Next, the cells were incubated for 24 h to permit cell attachment. Then, 200 μL of the hydrogel suspensions varying from 0.125 to 250, and 500 μg mL^{-1} in the culture medium were prepared by diluting Alg–Zn, Alg–HA–Zn, and Alg–HA–Zn–PDA solutions in the medium. The cells were incubated with the hydrogel solutions (n = 3, for each group) for another 24 h. After incubation for 48 and 72 h, the medium was replaced with 180 μL of fresh medium and 20 μL of MTT (5 mg in 1 mL PBS), following another incubation for 4 h, to allow the formation of formazan dye. The medium was removed and 150 μL of DMSO was added into each well to dissolve the purple formazan. Finally, the absorbance at 570 nm was measured using a microplate reader. The cell

viability percentage was determined by the following formula:

$$\text{cell viability}\,(\%) = \frac{A_s}{A_c} \times 100 \quad (10)$$

where A_s and A_c represent the absorbance of the sample and control group, respectively.

2.11. *In vitro* antibacterial and anti-biofilm studies

To assess the antibacterial activity of the hydrogels, *S. aureus* (ATCC25923) and *E. coli* (ATCC25922) were used. The spread plate method for colony counting of *E. coli* and *S. aureus* was employed for the antibacterial effect of the hydrogels. Bacteria were cultured in brain heart infusion (BHI) broth/agar (Merck, Germany) aerobically at 37 °C for 18–24 h. First, 20 μL of the bacterial suspension (1.5×10^8 CFU mL^{-1}) was added into 1 mL of the sterilized hydrogel groups. Then, the NIR-treated groups were irradiated under the NIR laser for 10 min (1 W cm^{-2}). After 2 h of incubation at 37 °C, the samples was further re-suspended and diluted 30 times. Then, 100 μL of the diluted solution was spread on a nutrient agar plate (Merck, Germany) and incubated for 18–24 h at 37 °C. Eventually, bacterial colonies were counted on each plate. Normal saline was determined as the control group. The bacterial survival ratio was measured by the following equation:

$$\text{Bacterial survival ratio (\%)} = (N \text{ in sample}/N \text{ in control}) \times 100 \quad (11)$$

where N is the colony number on a plate.

To determine the biofilm eradication ability of the hydrogels, briefly, 100 μL of *S. aureus* solution (10^6 CFU mL^{-1}) was placed in a 24 well plate and incubated at 37 °C. After 24 h incubation, LB medium was removed and the biofilm was washed with sterile PBS solution. The Alg–HA–Zn and Alg–HA–Zn–PDA hydrogels at different concentrations were added and incubated with the pre-formed biofilm for 2 h in the absence or presence of NIR treatment (1 W cm^{-2}, 10 min). After treatment, the biofilms were cleaned with PBS three times and the viability was evaluated by the crystal violet (CV) (HiMedia, India) staining method. To this end, the samples were fixed by absolute methanol and then, 0.2% (w/v) CV solution was added for 10 min. After that, the samples were washed three time by sterile PBS. Finally, the samples were dissolved with 33% (v/v) glacial acetic acid, and the absorbance of the extracted stains was measured at 590 nm. The biofilm + LB medium was used as the untreated sample.

Quantitative anti-biofilm analysis was calculated by:

$$\text{The anti-biofilm activity}\,(\%) = \frac{1 - \text{OD590 nm of treated}}{\text{OD590 nm of untreated}} \times 100 \quad (12)$$

2.12. Antioxidant activity

The free radical scavenging ability of the Alg–HA–Zn and Alg–HA–Zn–PDA hydrogels was studied using DPPH as the reactive nitrogen species (RNS) scavenger. This indicator is commonly used to evaluate the RNS scavenging capacity of antioxidant materials. To this end, different amounts of Alg–Zn, Alg–HA–Zn, and Alg–HA–Zn–PDA hydrogels (20, 30 and 40 mg) of 500 μM were immersed in 3 mL of ethanol. The resulting mixture was stirred in a dark place at room temperature for 30 min. Afterwards, the absorbance changes of the samples were detected by a UV-vis spectrophotometer. The DPPH scavenging effect was calculated by the following formula:

$$\text{DPPH scavenging}\,(\%) = \frac{A_b - A_s}{A_b} \times 100 \quad (13)$$

where A_b is the absorption of the blank (DPPH + ethanol), and A_s is the absorption of the sample (DPPH + sample + ethanol).

2.13. *In vitro* blood clotting index

50 mg powder of freeze-dried Alg–Zn, Alg–HA–Zn, Alg–HZ–Zn–PDA, and gauze were placed into pre-warmed experimental tubes at 37 °C. Next, anticoagulated human whole blood (100 μL) was dropped on the hydrogel surface, followed by adding $CaCl_2$ solution (12.5 μL, 0.2 M), to start coagulation. The tubes incubated at 37 °C. After 30, 60, 120, and 240 s, 10 mL of deionized water was added gradually into the tubes. The samples were centrifuged (1000 rpm, 5 min) and then the absorbance of the supernatant solution was measured at 540 nm using a microplate reader (infinite, M200, Austria). Blood without the hydrogel was considered as a reference. Finally, the percent of blood clotting index (% BCI) was obtained using the following equation:

$$\text{BCI}(\%) = \frac{A_s}{A_r} \times 100 \quad (14)$$

where A_s is the absorbance of the samples or gauze and A_r is the absorbance of the reference. Each experiment was repeated three times.

2.14. *In vivo* hemostatic study

A rat tail-amputation model was used to assess the hemostatic capacity of the hydrogels. All animal studies (including Section 2.14) were approved by the animal research Zanjan University of Medical Sciences Animal Ethics Committee (ZUMs, REC.1398.282). 20 Sprague-Dawley rats (male, 200–250 g) were randomly and equally divided into four groups. The animals were anesthetized by intraperitoneal (IP) injection of ketamine (50 mg mL^{-1})–xylazine (20 mg mL^{-1}) cocktail (0.25 mL, 6 : 4 v/v). Next, the middle of the tail was amputated by a surgical cutting tool. Then, the tail of the rat was placed in the air for 15 s to ensure normal blood loss. After that, the tail was covered by pre-weighed freeze-dried hydrogel powders (Alg–Zn, Alg–HA–Zn, and Alg–HA–Zn–PDA) to evaluate the hemostatic time and blood loss. The group without any treatment was used as the control.

2.15. *In vitro* wound healing (scratch assay)

NIH_3T_3 fibroblast cells were applied to investigate the *in vitro* wound healing activity of the hydrogels. NIH_3T_3 cells were cultured at a density of 5×10^5 cells per well in a 24-well plate overnight. Next, the cells were starved by DMEM, 0.1% FBS and

5% penicillin/streptomycin for 24 h, preventing the cells from proliferating to ensure that wound closure results solely from cell migration.[52] Then, an artificial wound was generated by a sterile 100 μL pipet tip in the middle of each well and the cell debris was removed by the culture medium. Next, a 500 μL suspension of Alg–HA–Zn and Alg–HA–Zn–PDA hydrogels (300 μg mL^{-1}) in DMEM, supplemented by 10% FBS and 5% penicillin/streptomycin was added into each well plate. The sample without any treatment was applied as a control group. The scratch healing process of each group at 0, 10, and 24 h was re-photographed by a phase contrast microscope. The scratch healing area percentage was calculated using the following formula:

$$\text{Scratch area}(\%) = \frac{A_n}{A_0} \times 100 \quad (15)$$

where, A_0 is the scratch area at 0 h and A_n is the area at other times.

2.16. *In vivo* wound healing study

A full-thickness cutaneous infected wound model was employed to evaluate the healing ability of the Alg–HA–Zn and Alg–HA–Zn–PDA (±NIR) hydrogels. First, healthy rats (male, 180–200 g) were randomly divided into four groups, *i.e.*, control, Alg–HA–Zn, Alg–HA–Zn–PDA (−NIR), and Alg–HA–Zn–PDA (+NIR). The rats were anesthetized by IP injection of ketamine (50 mg mL^{-1})–xylazine (20 mg mL^{-1}) cocktail (0.25 mL, 6 : 4 v/v) and shaved on the dorsal region. Then, rounded full-thickness wounds (diameter: 1.2 cm) were created. After that, 20 μL of *S. aureus* suspension ($\sim 10^8$ CFU mL^{-1}) was added to each wound site. All groups were subjected to the following different treatments. In the NIR groups, the wounds were exposed under NIR laser (808 nm, 1 W cm^{-2}) after adding the hydrogels for 5 min and maintained at 42 °C. The regeneration process of the wounds was assessed by wound area monitoring. The wounds were photographed on days 0, 3, 6, 8, 11 and 13. The wound dressings were replaced on the 2nd and 4th days. Image J software was used to analyze the wound area. Wound closure was measured according to the formula:

$$\text{Wound area}(\%) = \frac{A_n}{A_0} 100 \quad (16)$$

where, A_0 and A_n are the wound areas on day 0 and at different times, respectively.

2.17. Histopathological analysis

To evaluate epidermal regeneration and inflammation in the wound site, wound tissues were collected on the 7th and 15th days. First, the cutaneous tissues were fixed in a 10% neutral buffered formalin solution, dehydrated (using ascending alcohols), clarified with xylene, and then paraffin-embedded. Then, the samples were sectioned into 5 μm thick slices and subsequently, stained with hematoxylin or eosin (H&E) and Masson's trichrome. All cutaneous tissue slices were examined by a microscope, Dino-Lite camera, and Dino-capture software (V.2).

2.18. *In vivo* biocompatibility

The Sprague-Dawley rats (male, 250 g) were randomly divided into 2 groups (n = 4), Alg and Alg–HA–Zn–PDA. The rats were anesthetized by IP injection of ketamine (50 mg mL^{-1})–xylazine (20 mg mL^{-1}) cocktail (0.25 mL, 6 : 4 v/v) and shaved on the dorsal region. 200 μL of sterilized Alg and Alg–HA–Zn–PDA hydrogels were injected subcutaneously under the rat's dorsal skin. After 7 and 21 days, the rats were sacrificed and the cutaneous tissues were collected and embedded in formaldehyde 4%. The samples were studied using H&E staining to assess their *in vivo* biocompatibility.

2.19. Statistical analysis

The experimental data were expressed as mean ± standard deviation (SD). Statistical differences were conducted by a general linear model and one-way ANOVA followed by the Bonferroni test for multiple comparisons and t-test with SPSS, version 25 (IBM). In all cases, $p < 0.05$ was considered statistical significance.

3. Results and discussion

3.1. Characterizations of Alg–HA–Zn and Alg–HA–Zn–PDA hydrogels

The synthesis of the Alg–HA–Zn–PDA hydrogel was done through a simple mixing process, as shown in Fig. 1. FDA-approved Alg and HA natural polysaccharides were selected for the skeleton of the Alg–HA–Zn–PDA hydrogel. First, Alg and HA solutions were mixed with PDA and the Alg–HA–Zn–PDA hydrogel was prepared by adding Zn^{2+} as a cross-linker. The cross-linking is attributed to the interaction of the Zn^{2+} ion with the carboxyl and hydroxyl groups of the polymer.[53] The particle size and morphology of the prepared PDA NPs was investigated by scanning electron microscopy (SEM) (Fig. 2A and B). As shown, the nanostructures had spherical morphology with an average particle size of ~185 nm. The average zeta potential of the PDA NPs was measured to be −21.3 mV, which was similar to previous studies.[6] The surface morphology of the supramolecular hydrogels was studied by SEM, exhibiting the porous structure of the hydrogels (Fig. 2D). In addition, the existence of Zn^{2+} ions in the hydrogel was confirmed by energy dispersive spectroscopy (EDS), indicating a uniform distribution of the metal ions in the hydrogel (Fig. 2E).

The amount of water content of the Zn-incorporated hydrogels was measured and compared with each other. The results indicated that all hydrogels had the same water content and exhibited a high water content of ~95% (Fig. 2A).[54] FTIR spectroscopy was used for the confirmation of the hydrogel formation by Zn and PDA NPs incorporation *via* the recognition of the surface functional groups of the hydrogels in the range 4000–400 cm^{-1} (Fig. 2B). Alg showed a broad band at 3400 cm^{-1} attributed to O–H stretching vibrations.[55] A modest band at 2900 cm^{-1} could be related to the C–H stretching vibrations of Alg. The FTIR spectra also exhibited bands at 1600 and 1400 cm^{-1}, which are assigned to the asymmetric and

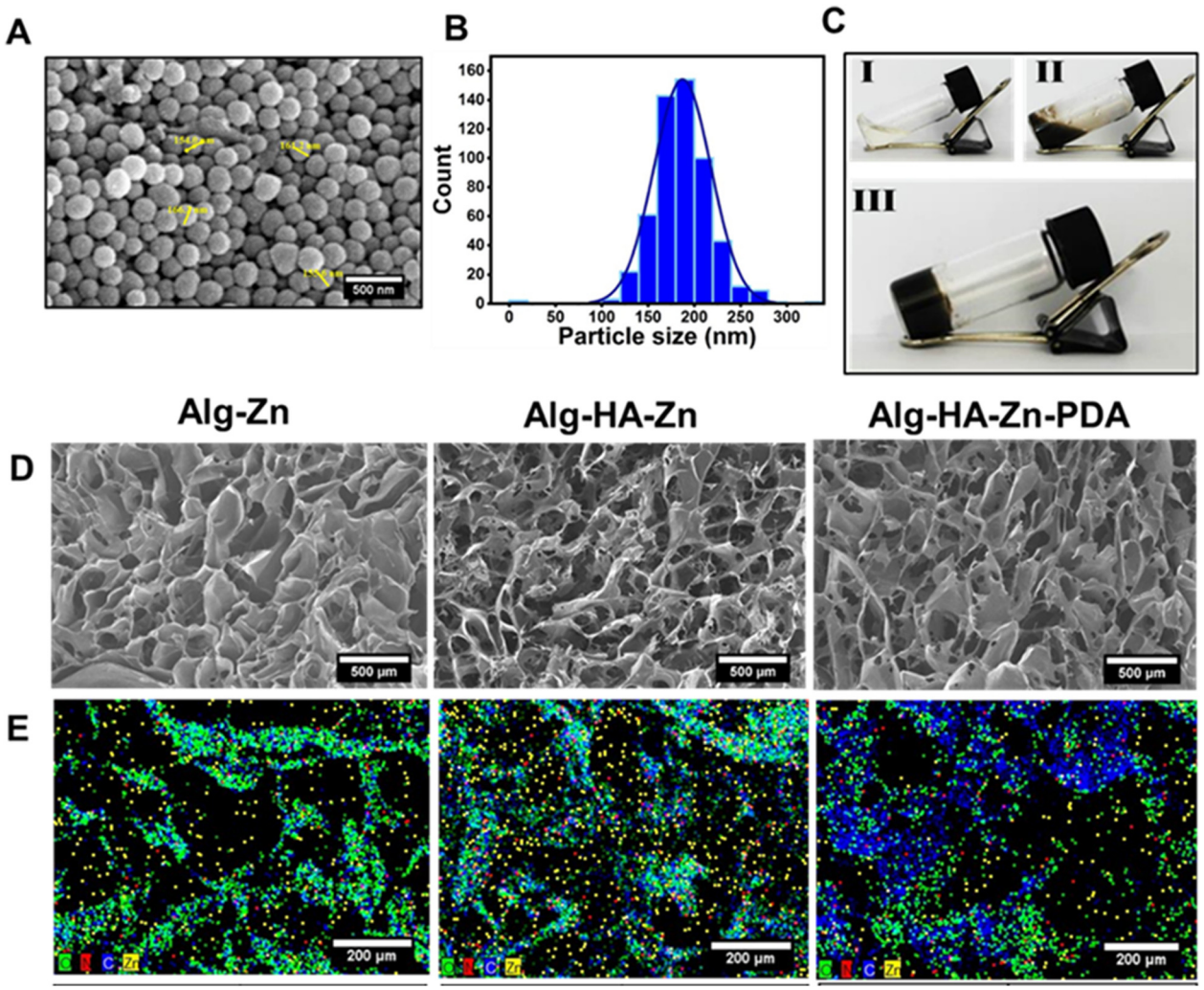

Fig. 2 The morphology and structure evaluation of PDA NP, Alg–Zn, Alg–HA–Zn and Alg–HA–Zn–PDA hydrogels. (A) SEM image of PDA NPs, scale bar: 500 nm. (B) Size distribution of PDA NP. (C) Digital photograph of (I) Alg–HA, (II) Alg–HA–PDA, and (III) Alg–HA–Zn–PDA. (D) SEM image of Alg–Zn, Alg–HA–Zn, and Alg–HA–Zn–PDA hydrogels, scale bar: 500 μm. (E) Elemental mapping of the hydrogels, scale bar: 200 μm.

symmetric carboxylate group (COOH) stretching vibrations on the polymeric backbone of Alg, respectively.[56] For Alg–Zn hydrogels, the carboxyl groups are functionalized by metal ions, and the absorption bands shifted to 1700 and 1500 cm^{-1}. Also, the band at 530 cm^{-1} in the Alg–Zn hydrogel spectrum is attributed to the metal–oxygen bonds.[57] For the pure PDA NPs, the peak around 3369 cm^{-1} corresponds to the stretching vibration of phenolic O–H and N–H groups, the band at 1584 cm^{-1} contributes to the stretching and bending vibration of N–H, and a small peak at 1290 cm^{-1} is assigned to the stretching vibration of phenolic C–O.[58–60] In the FTIR spectra of HA, a broad peak centered at 3600 cm^{-1} can be assigned to O–H stretching vibrations. The peaks at 1610 and 1430 cm^{-1} were related to the asymmetric and symmetric carboxylate group (COOH) stretching vibrations.[61]

The peak at 530 cm^{-1} in the Alg–Zn, Alg–HA–Zn, and Alg–HA–Zn–PDA hydrogel spectra is attributed to the oxygen–metal bond, which is considered a characteristic peak in the Zn-cross-linked hydrogels.[57] In addition, the spectra of the pure compounds (Zn, Alg, and HA) broadened and shifted to higher wavenumbers after the fabrication of Alg–HA–Zn–PDA. These results can confirm the successful fabrication of the hydrogel through attractive interaction between the functional groups of the hydrogel by hydrogen bonding and coordinative interactions.[62,63] The XRD patterns of Alg, HA, PDA, Zn salt, Alg–Zn, Alg–HA–Zn, and Alg–HA–Zn–PDA hydrogels are presented in Fig. 3C. The XRD pattern of Alg and HA did not show crystal peaks because these polymers are amorphous.[64] PDA NPs showed a broad peak in the 2θ range of 12°–32°, suggesting its amorphous nature,[65] whereas the characteristic sharp peaks of the Zn cross-linker at 25, 30, 35, 37, 57, 63, and 68° were present in the spectra, corresponding to different crystal planes of the metal ion.[66] As shown, the strong peaks of Zn ions disappeared from the diffractograms of the Alg–Zn, Alg–HA–Zn, and Alg–HA–Zn–PDA hydrogels, which shows an interaction between the polymeric network and the metal ions.[67] The pyrolysis behaviors of the hydrogels and their constituents were investigated by thermogravimetric analysis (TGA) (Fig. 3D–F).

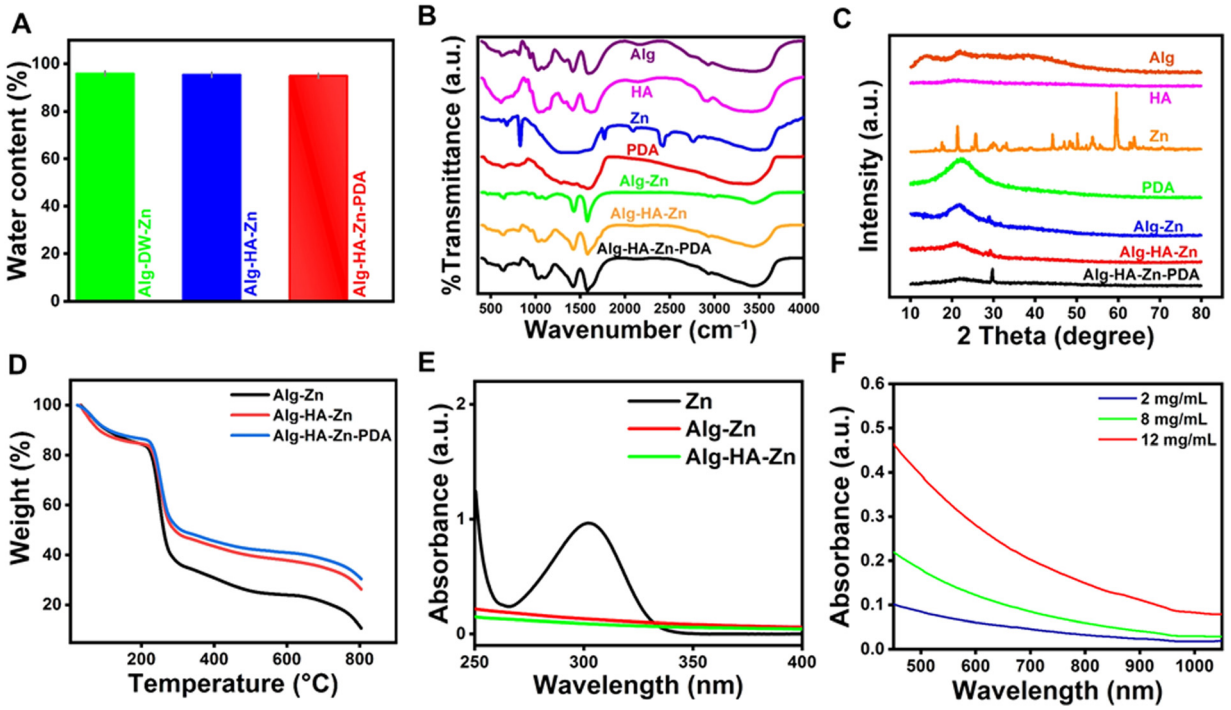

Fig. 3 Physicochemical characterization of the hydrogels. (A) Water content percentage of the hydrogels. (B) FTIR spectra and (C) XRD profile of the hydrogels and the raw materials. (D) TGA analysis of Alg–Zn, Alg–HA–Zn, and Alg–HA–Zn–PDA. (E) UV-visible absorbance spectra of Alg–HA–Zn, Alg–Zn, and zinc nitrate. (F) UV-visible-near infrared absorption spectra of the Alg–HA–Zn–PDA hydrogel at different concentrations (2, 8 and 12 mg mL^{-1}) in the visible and NIR range.

In all samples, the first weight loss at 30–200 °C is attributed to water evaporation.[68] The thermal decomposition behaviors of zinc nitrate,[69] HA,[70] PDA,[71] and Alg[72] are similar to the previously reported studies (Fig. S1, ESI†). After adding Zn^{2+}, thermal decomposition of the Alg–Zn, Alg–HA–Zn, and Alg–HA–Zn–PDA shifted to high-temperature values slightly, confirming gelation of the polymeric mixture by the cross-linker. UV-visible spectra were used to study the interaction of the metal cross-linker with the polymeric network. The absorbance band at ~310 nm is attributed to zinc ions.[41,73] The disappearance of the absorbance band can be assigned to the complexation of the polymers with Zn^{2+} ions in Alg–Zn and Alg–HA–Zn (Fig. 3E). The optical property of Alg–HA–Zn–PDA was characterized by UV-visible-near infrared absorption spectroscopy. The absorption spectra of the hydrogel covered the NIR-I region (Fig. 3F). The hydrogel had an absorbance in the range of the NIR wavelength between 700 and 900 nm, which was concentration dependent as well, suggesting NIR activity of the hydrogel stemming from the PDA NPs.[74] The energy dispersive X-ray (EDX) spectrum provided further evidence for the co-existence of O (49.61%), C (45.20%), N (3.77%), and Zn (1.42%) in the Alg–HA–Zn–PDA hydrogel (Fig. S2, ESI†).

3.2. The rheological properties of the hydrogels

The cross-linked structure and microstructural changes of the hydrogels were studied by dynamic rheometry. The frequency sweep test was conducted at a constant strain amplitude of 0.5% from 0.01 to 100 Hz. As shown, Alg–Zn, Alg–HA–Zn, and Alg–HA–Zn–PDA exhibited higher storage modulus (G') values than loss modulus (G''), confirming that the hydrogels had more elastic properties, thus showing gel-like behavior (Fig. 3A–C).[75] In addition, the G' value of the Alg–HA–Zn–PDA hydrogel was slightly larger than that of the Alg–Zn and Alg–HA–Zn hydrogels, indicating further attractive interactions within the hydrogels after introducing PDA NPs (Fig. 3D). The strain sweep test of the Alg–HA–Zn–PDA hydrogel showed that the hydrogel had fluid-like properties when the G'' value was higher than G', indicating fluidity of the hydrogel and potential ability of the hydrogel to fill irregular wound shapes (Fig. 3E).[76] In addition, the changes of viscosity *versus* shear rate for Alg–Zn, Alg–HA–Zn, and Alg–HA–Zn–PDA were measured (Fig. 3F). As shown, all hydrogels exhibited a drop in viscosity with increasing shear rate that can be attributed to the disruption of the fragile intercluster entanglements and shear-thinning behavior.[77] These results confirmed that the hydrogels had excellent shear thinning properties, which is a very important factor to construct injectable hydrogels for wound healing applications.[78] The injectability of the hydrogel was further assessed by injecting it from a 27-G syringe (Fig. 4F). Due to the shear thinning property of the hydrogel it could be injected to draw "ZUMS", which had a good potential for injectable wound healing applications.

3.3. Swelling, degradation, and Zn ion release studies

Gravimetric analysis was used to measure the swelling profile of the Alg–HA–Zn–PDA hydrogel (Fig. S3, ESI†). The good

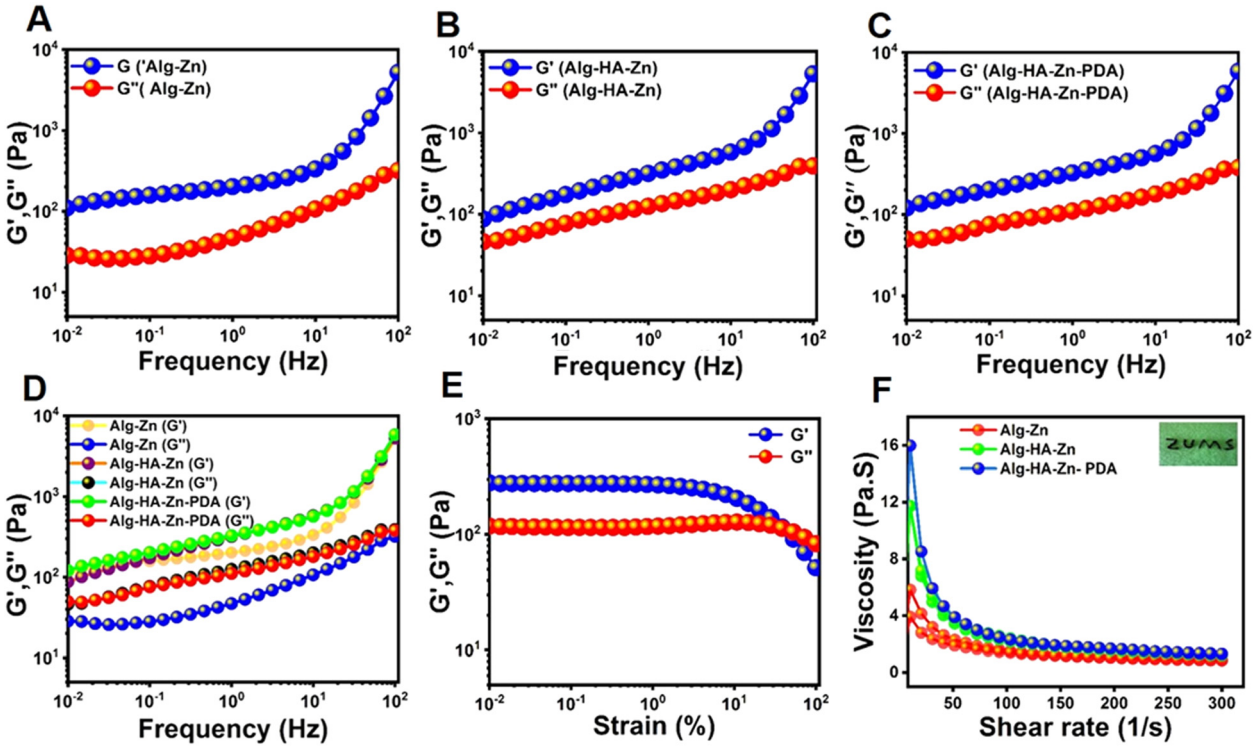

Fig. 4 The rheological analysis of the hydrogels. Frequency sweep test of (A) Alg–Zn. (B) Alg–HA–Zn. (C) Alg–HA–Zn–PDA. (D) Rheological performance of the all hydrogels with the frequency sweep test. (E) Strain sweep test of the Alg–HA–Zn–PDA hydrogel, changing the strain from 0.01% to 100%, with a constant frequency of 10 rad s^{-1}. (F) Shear thinning test of the Alg–Zn, Alg–HA–Zn, and Alg–HA–Zn–PDA hydrogels (inset shows injectable properties presentation of Alg–HA–Zn–PDA).

swelling property of Alg–HA–Zn–PDA endows the hydrogel with the capabilities to effectively absorb tissue exuded and maintain a wet environment during the wound repair process. The degradation property of a hydrogel is of particular importance for consideration in tissue regeneration. The *in vitro* gel degradation assay was carried out in PBS (pH 7.4). Our results showed that the hydrogel had 63.4% degradation after 2 h. As shown in Fig. S3 (ESI†), the degradation of Alg–HA–Zn–PDA increased over time. The concentration of Zn^{2+} released from Alg–HA–Zn–PDA was determined by atomic absorption spectroscopy. As the concentration increased, the amount of Zn^{2+} increased. As shown in Fig. S4 (ESI†), the cumulative concentration of released Zn^{2+} from Alg–HA–Zn–PDA after 5 h was 1.5 mg mL^{-1}. After ~12 h the amount reached a plateau. This observation was in good agreement with the degradation profile of the hydrogel.

3.4. Photothermal properties of the Alg–HA–Zn–PDA composite hydrogel

The photothermal activity of the PDA NPs and Alg–HA–Zn–PDA hydrogel was studied under irradiation with 808 nm light. As shown in Fig. 4A, when the power density was 0.5, 1, and 1.5 W cm^{-2}, the final temperature of the PDA NPs reached about 42, 55, and 58 °C after 10 min, respectively. For the Alg–HA–Zn–PDA hydrogel, the temperature increased when the power density and the amount of PDA (5 μL and 10 μL) in the Alg–HA–Zn–PDA hydrogel increased (Fig. 4B and C). Moreover, the thermal stability test of the Alg–HA–Zn–PDA hydrogel exhibited a stable on–off effect after four cycles of NIR irradiation (Fig. 4D). Fig. 4E represents the photothermal response of the Alg–HA–Zn–PDA hydrogel after one heating–cooling cycle. In addition, our results showed that the negative natural logarithm of temperature correlated well with the cooling time (Fig. 4F). Furthermore, using the τs obtained, the photothermal conversion efficiency of the Alg–HA–Zn–PDA hydrogel was measured to be 21%, which was sufficient to implement a PTT.[3] Fig. 5G shows IR thermal images of the Alg–HA–Zn–PDA hydrogel under continuous irradiation with NIR light for 10 min. These thermal images demonstrated that the NIR activity of the Alg–HA–Zn–PDA hydrogel was time-dependent. In contrast, the IR thermal images of Alg–HA–Zn did not exhibit a significant change in temperature when the illumination time increased (data was not shown). These findings indicated that the PDA-loaded hydrogel could absorb and convert 808 nm light into heat efficiently. According to the photothermal results, the strong NIR absorption and favorite photoactivity performance make Alg–HA–Zn–PDA hydrogel highly promising for photothermal therapeutic applications (Fig. 5).

3.5. Hemocompatibility, cytocompatibility, and cell migration studies of the hydrogels

Hemocompatibility is a fundamental *in vitro* assay to evaluate the interaction of NPs/hydrogels with red blood cells (RBCs). Hemolysis induces changes in the membrane integrity of RBCs,

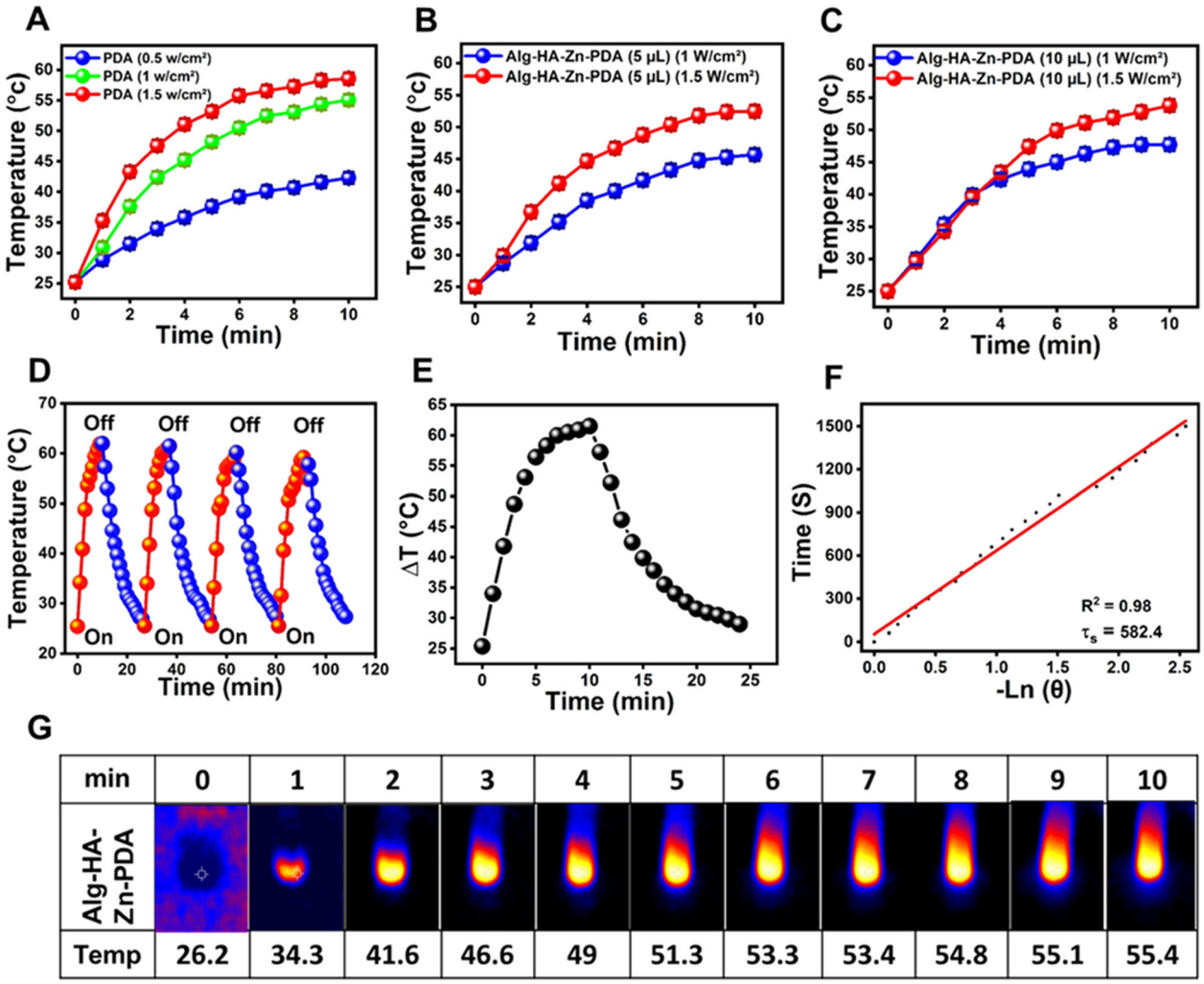

Fig. 5 Photothermal performance of the Alg–HA–Zn–PDA hydrogel induced by NIR laser. (A) Temperature evaluation of the PDA NPs irradiated by an 808 nm laser at different powers. (B) and (C) Temperature evaluation of the Alg–HA–Zn–PDA hydrogel irradiated by an 808 nm laser at different powers and with different amounts of PDA NPs. (D) Photo stability profile of the Alg–HA–Zn–PDA hydrogel. (E) The photo thermal response of the Alg–HA–Zn–PDA hydrogel with a NIR laser (808 nm, 1.5 w cm^{-2}) for 10 min and the cooling phase of 15 min. (F) Linear time data *versus* $-\ln\theta$ measured by the cooling period of Fig. 4e. (G) The NIR thermal images of the Alg–HA–Zn–PDA hydrogel for 10 min (808 nm, 1.5 w cm^{-2}).

which can cause discharge of hemoglobin (Hb).[46] The hemocompatibility of the Alg–HA–Zn and Alg–HA–Zn–PDA hydrogels was studied by hemolysis test.[51] Fig. 6A and B indicate that Alg–HA–Zn and Alg–HA–Zn–PDA hydrogels did not cause any RBC lysis, indicating good hemocompatibility of the hydrogels. The picture in Fig. S5 (ESI†) exhibited an apparent difference in color among the hydrogel group, positive control group (water), and negative control group (PBS; pH ~7.4). As shown, RBCs treated with Alg–HA–Zn and Alg–HA–Zn–PDA hydrogels remained intact and the supernatant of the samples was colorless. In contrast, the supernatant of the positive group was bright red. These results proved the high hemocompatibility of the hydrogels, which is an essential criterion for biomaterials to be used in biomedical applications. Fibroblast cell line NIH-3T3 was used to further investigate the cytocompatibility of the hydrogels. As shown in Fig. 6C, the hydrogels presented no significant difference in cytotoxicity to NIH_3T_3 cells at 24 h and 48 h. For the Alg–HA–Zn–PDA group, the cell viability significantly increased after 24 h of incubation, indicating that the hydrogel was favorable for cell growth. Although such an increase in cell growth was higher than the control group after 24 h, it was not statistically different (Fig. 6C). All these results demonstrated that these hydrogels possess good potential for wound healing applications.

The scratch assay of the NIH_3T_3 fibroblast cells was performed to evaluate the cell migration capability in the culture medium as the control group, as well as treatment with Alg–HA–Zn and Alg–HA–Zn–PDA hydrogels. Due to their crucial role in wound repair, the fibroblast cells were used in the experiment. Migrations of NIH_3T_3 cells were evaluated at 0 h, 10 h, and 24 h. Our results revealed that the hydrogels containing Zn and PDA had a noteworthy influence on cell migration. Compared with the control group which had 46.01% cell migration ratio, the Alg–HA–Zn–PDA group showed the largest

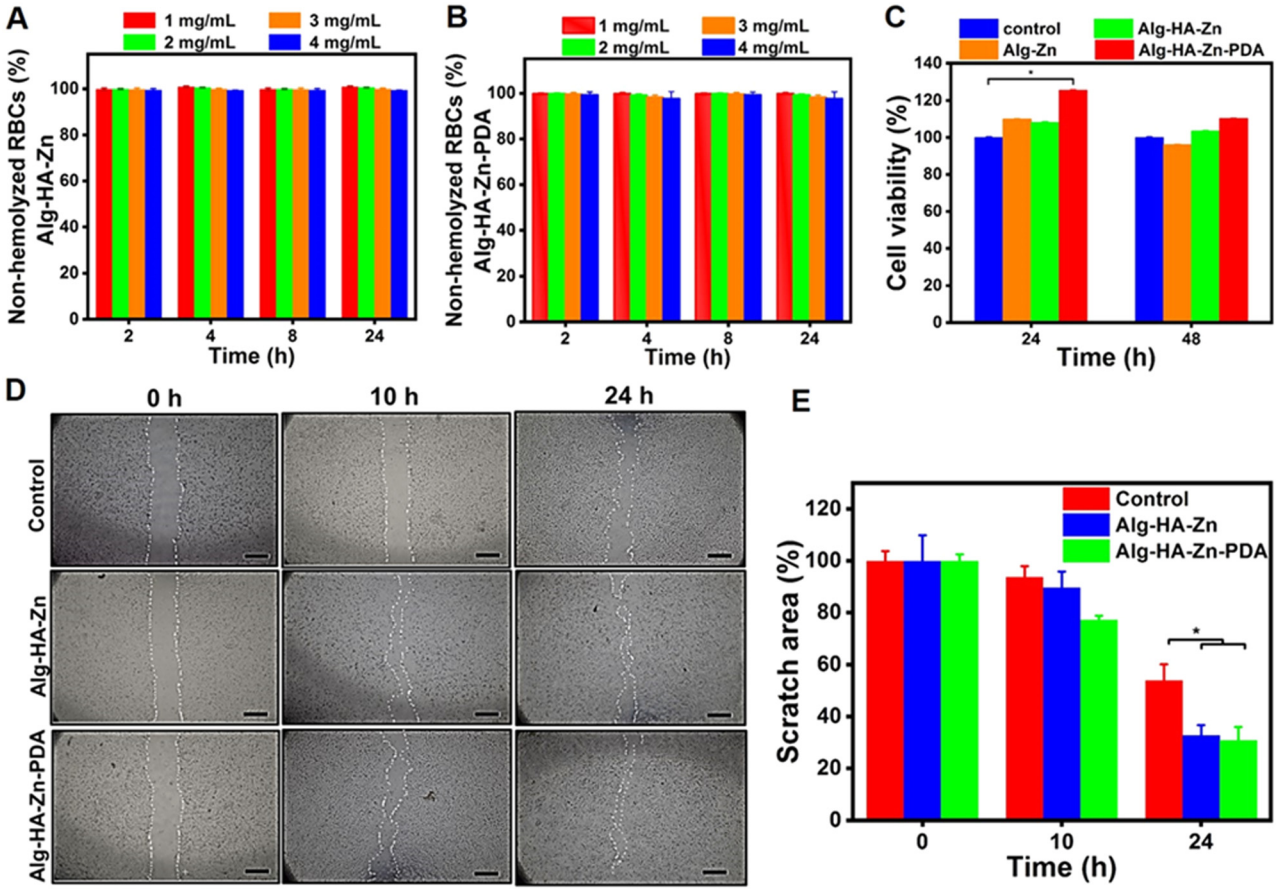

Fig. 6 Non-hemolyzed ratio of (A) Alg–HA–Zn, and (B) Alg–HA–Zn–PDA, (mean ± SD, n = 3). (C) *In vitro* cell viability assay of the hydrogels at 24 and 48 h, (mean ± SD, n = 3, *$p < 0.05$). *In vitro* wound repair study. (D) The supplied photograph of NIH_3T_3 cell migration *via* the scratch healing assay at 0, 10, and 24 h. (E) Scratch area % of the hydrogels and non-treatment group (control); (mean ± SD, n = 3, *$p < 0.05$).

migration ratio of 69.15% (Fig. 6D). In addition, the corresponding photographs also displayed that after 10 h and 24 h, the cells treated with Alg–HA–Zn and Alg–HA–Zn–PDA showed obvious migration (Fig. 6E). It has been demonstrated that porous and biocompatible hydrogels could help the cell migration and proliferation during the wound healing process. In addition, the zinc ions released from the hydrogels could promote cell proliferation and migration, thus potentially enhancing *in vitro* wound repair.[41] Furthermore, many studies are revealing that Alg and HA could enhance cell proliferation and migration.[79]

3.6. *In vitro* antibacterial and antibiofilm activity of the hydrogels

The antibacterial capability of the Alg–HA–Zn and Alg–HA–Zn–PDA hydrogels against *E. coli* and *S. aureus* was investigated with/without 808 nm laser irradiation. Fig. 7A and 7B presents the viable colonies of *E. coli* and *S. aureus* growing well on agar plates without 808 nm light irradiation. The viability of *E. coli* and *S. aureus* was calculated to be 21.5% and 69.9%, respectively, when Alg–HA–Zn hydrogel was used as an antibacterial agent. This finding highlights the possible role of Zn^{2+} ion release from the hydrogel to kill the bacteria. However, there was no statistically significant difference between the viabilities in the presence of NIR light irradiation. In the case of Alg–HA–Zn–PDA, the viability of *E. coli* and *S. aureus* was 15.4% and 63.6%, respectively, whereas the viability of *S. aureus* further decreased to 19.2% in the presence of NIR irradiation. Noticeably, 100% of *E. coli* eradication was observed when the light was applied (Fig. 7C and D). This result indicated that the generated heat and release of zinc ions from the NIR-active hydrogels can be responsible for the antibacterial property of the hydrogels. Such heat generation and ion release can lead to bacterial death *via* denaturation of the enzymes and destruction of the proteins and lipids on the bacteria cell membranes.[76,80,81]

The wound healing process becomes more challenging when bacterial biofilms are formed. This type of resistant bacteria contains proteins, exopolysaccharides, and extracellular DNA. The dense biofilm matrix increases antibiotic resistance and thus has the potential to delay wound repair.[82,83] The antibiofilm effect of Alg–HA–Zn and Alg–HA–Zn–PDA against *S. aureus* under NIR irradiation was investigated (Fig. S6, ESI†).

Biofilm inhibition (%) of Alg–HA–Zn and Alg–HA–Zn–PDA hydrogels against *S. aureus* under NIR irradiation was measured to be 1.1% and 28.4%, respectively. Such activity again

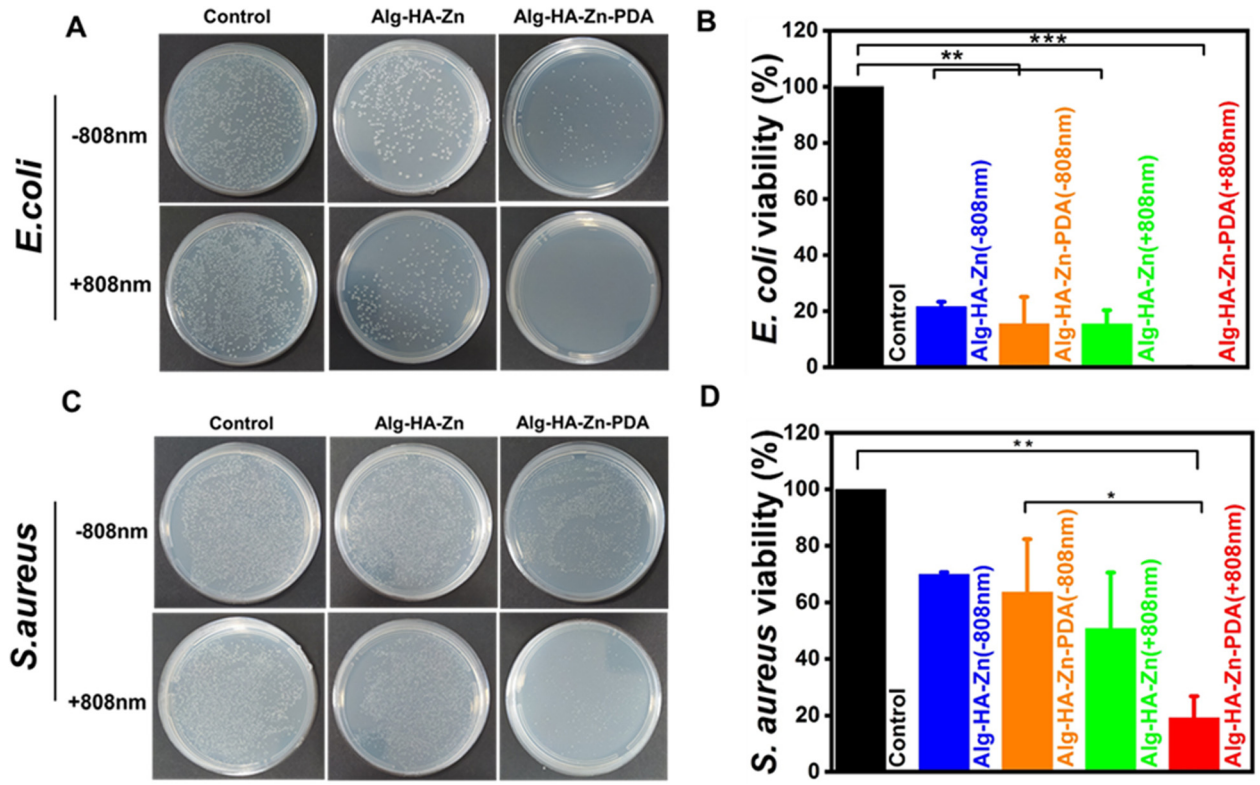

Fig. 7 Antibacterial activities. (A) and (B) Photographs of the growth of *E. coli* colonies on an agar plate with and without NIR irradiation after 24 h incubation, and their corresponding viability (%). (C) and (D) Photographs of the growth of *S. aureus* colonies on an agar with and without NIR irradiation after 24 h incubation and their corresponding viability (%), (mean ± SD, $n = 3$, $^{*}p < 0.05$, $^{**}p < 0.01$, $^{***}p < 0.001$).

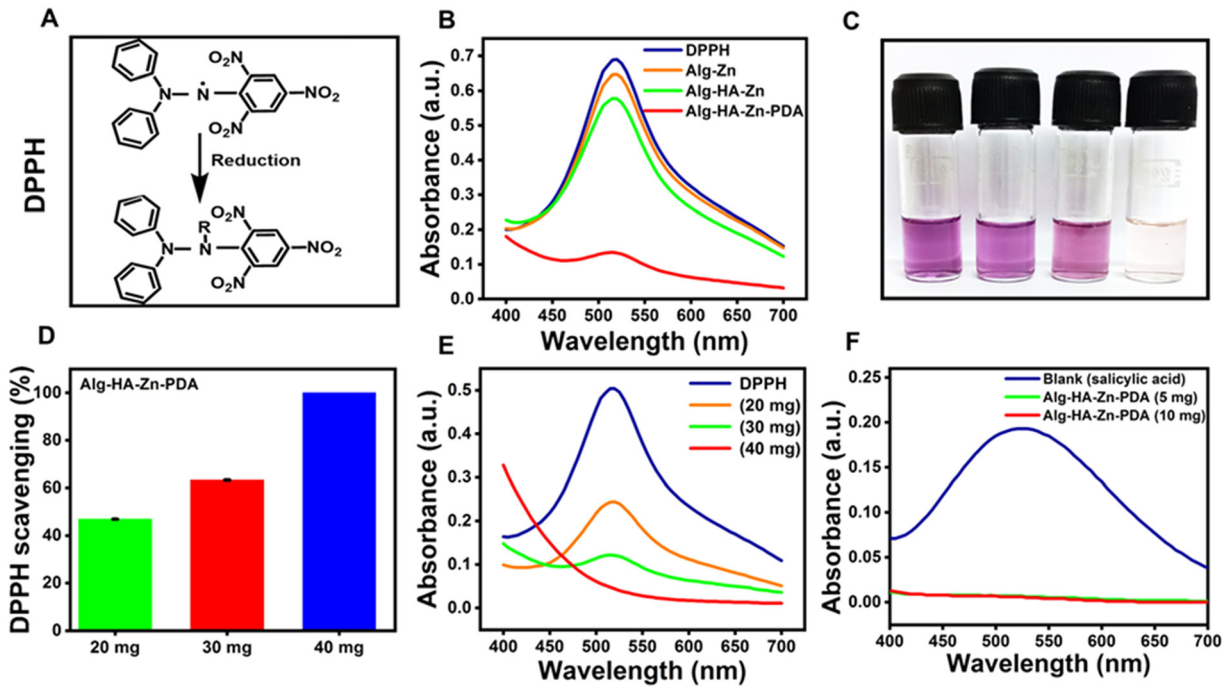

Fig. 8 Antioxidant activity of the hydrogels. (A) Mechanism of DPPH scavenging assay. (B) The UV-vis spectra of DPPH after co-incubation with the hydrogels. (C) Photograph of the DPPH assay solutions. (D) DPPH scavenging ratio of 20, 30 and 40 mg of Alg–HA–Zn–PDA. (E) DPPH assay absorbance curve of different amounts of Alg–HA–Zn–PDA and DPPH. (F) Antioxidant activity of the hydrogel by using salicylic acid (mean ± SD, $n = 3$).

indicated the impact of the produced heat on the antibiofilm activity of the PDA-loaded hydrogel.

3.7. Free radical scavenging capacity

Oxidative stress resulting from the production of free radicals can cause the peroxidation of lipids, damage to DNA, and inactivity of enzymes. Therefore, the application of a wound-healing compound with the property of free radical scavenging on patients or animals leads to significant improvement of wound repair.[84,85] As depicted in Fig. 8A, the free radical scavenging capacity of the hydrogels was investigated through DPPH, which is widely used as a model molecule to assess the scavenging efficiency of antioxidant compounds.[75] After the reaction of Alg–Zn or Alg–HA–Zn hydrogels with DPPH solution, a decreased absorption peak was detected in the tested hydrogels. Interestingly, when Alg–HA–Zn–PDA was used as an antioxidant hydrogel, there was no absorbance peak at 517 nm and a complete color loss of the DPPH solution occurred (Fig. 8B and C). The significant antioxidant property of Alg–HA–Zn–PDA can mainly be attributed to PDA. Dopamine-based materials with many catechol groups can scavenge ROS by the reductive functional groups, endowing the Alg–HA–Zn–PDA hydrogel with potent antioxidant properties.[28] The DPPH scavenging property of the Alg–HA–Zn–PDA hydrogel showed a concentration-dependent behavior. As shown in Fig. 8D different concentrations of Alg–HA–Zn–PDA hydrogel showed various degrees of free radical scavenging efficiency. When the hydrogel amount increased from 20 to 30 mg, the scavenging percentage

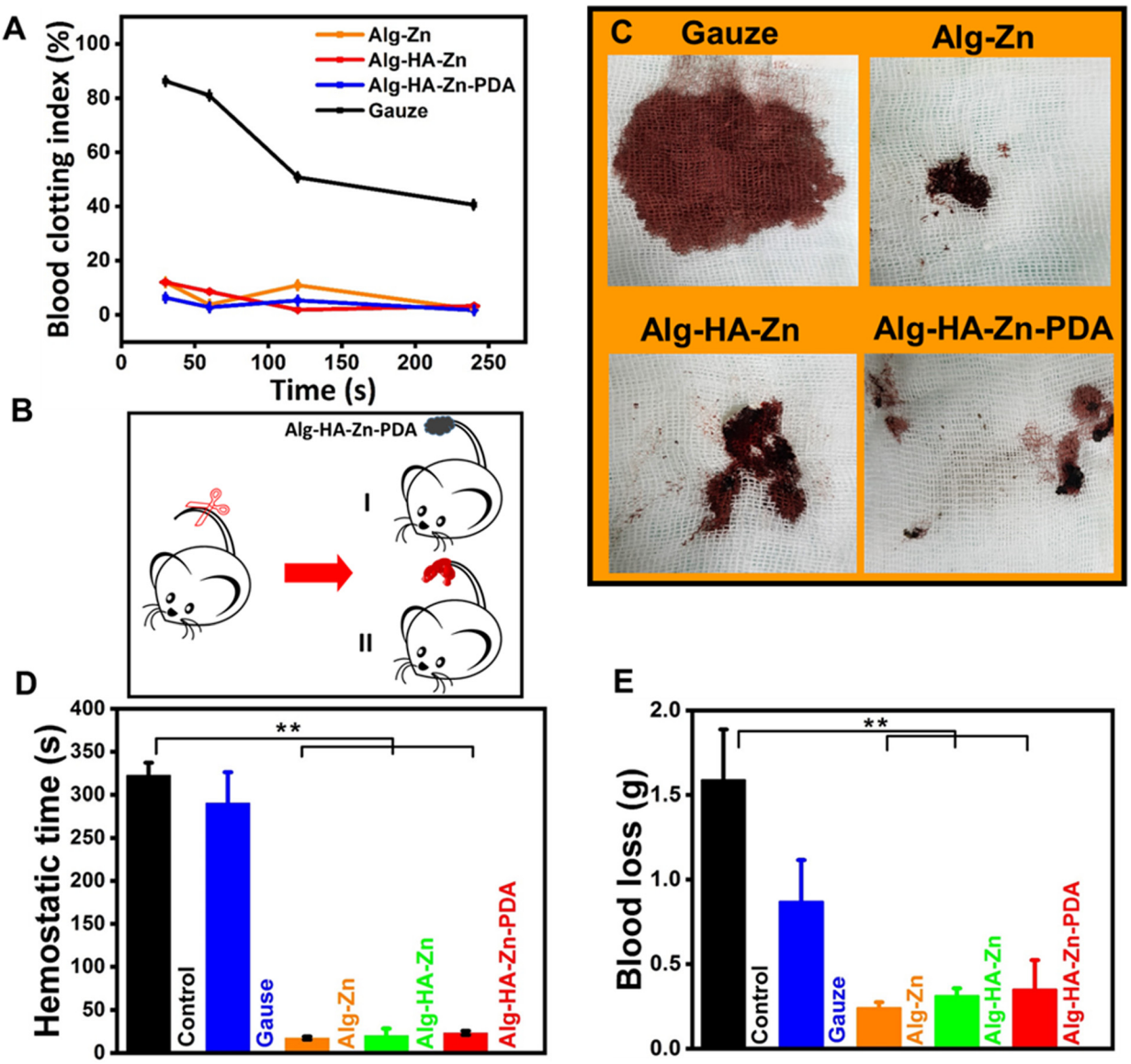

Fig. 9 Hemostatic capacity of the hydrogels. (A) *In vitro* dynamic whole blood-clotting (BCI) index of the hydrogels compared with gauze and the control (untreated), (***$p < 0.001$, **$p < 0.01$ and *$p < 0.05$ between 30, 60, 120 and 240 s, respectively). (B) Schematic representation of the rat-tail amputation model: I and II are with and without Alg–HA–Zn–PDA as a hemostatic agent. (C) Bloodstain photographs of the rat-tail amputation model. (D) Hemostatic time and (E) blood loss in the rat tail-amputation model, ***$p < 0.001$, (mean ± SD, $n = 5$).

gradually increased from 46% to 63%. However, 40 mg of the hydrogel was able to scavenge almost all free radicals (Fig. 8D and E). In addition, we evaluated the antioxidant property of the Alg–HA–Zn–PDA hydrogel using salicylic acid as an indicator as well. As shown in Fig. 8F, the same results were obtained for the scavenging of salicylic acid in pure salicylic acid and the hydrogels. The quantity of salicylic acid absorbance reduced noticeably in the Alg–HA–Zn–PDA hydrogel compared to pure salicylic acid. Generally, according to previous studies, the structure of catechol exists in a variety of natural antioxidants and can scavenge ROS.[86] Therefore, PDA incorporation into Alg–HA–Zn confers the hydrogels with good antioxidant properties, which is in line with reports in other studies.[87,88]

3.8. *In vitro* blood clotting and *in vivo* hemostatic evaluation of the hydrogels

Hemostasis is the first step in the healing of a skin injury.[89] Alg has been reported to have an antibleeding effect, and due to the adhesive capacity of Alg–HA–Zn–PDA, stemming from PDA, we studied the hemostatic property of the hydrogel. *In vitro* blood clot index (BCI) was used to assess the blood clotting ability of gauze as the control group, as well as the Alg–Zn, Alg–HA–Zn, and Alg–HA–Zn–PDA hydrogels.[28] As shown in Fig. 9A, the BCI value of all hydrogels was significantly less than that of the control group at all studied time points (30, 60, 120 and 240 s). (***$p < 0.001$, *$p < 0.01$ and *$p < 0.05$ for 30, 60, 120 and 240 s, respectively.) These results confirmed the strong blood clotting effect of the hydrogels.

As for *in vivo* testing, a rat-tail amputation model was used to evaluate the hemostatic capacity of the hydrogels[90] (Fig. 9B and C). Our findings revealed that Alg-based hydrogels had more significant hemostatic ability compared to the gauze group (Fig. 9C). In addition, the hydrogels significantly reduced the bleeding in less than 30 s. In contrast, the gauze as a dressing required ~290 s to stop the bleeding (Fig. 9D and E). The blood loss during the hemostatic process was recorded in the rat-tail amputation model as well. The quantitative analysis revealed that the group treated with the hydrogels exhibited significantly reduced blood loss (~0.2, 0.3, and 0.3 g for Alg–Zn, Alg–HA–Zn, and Alg–HA–Zn–PDA, respectively) compared to the gauze (0.8 g) and the non-treated (1.5 g) groups. The results demonstrated that the hydrogels had effective *in vivo* hemostatic capacity. The anti-bleeding effect of the hydrogels can be attributed to the hemostatic function of Alg,[91] Zn,[92] and PDA.[28] It has been reported that zinc can affect plasma clotting factors and aggregation of platelets, thus influencing the hemostasis process.[92] In addition, catechol and quinone groups on Alg–HA–Zn–PDA can interact with amino or thiol groups on the proteins, thus causing a physical barrier to bleeding.[28]

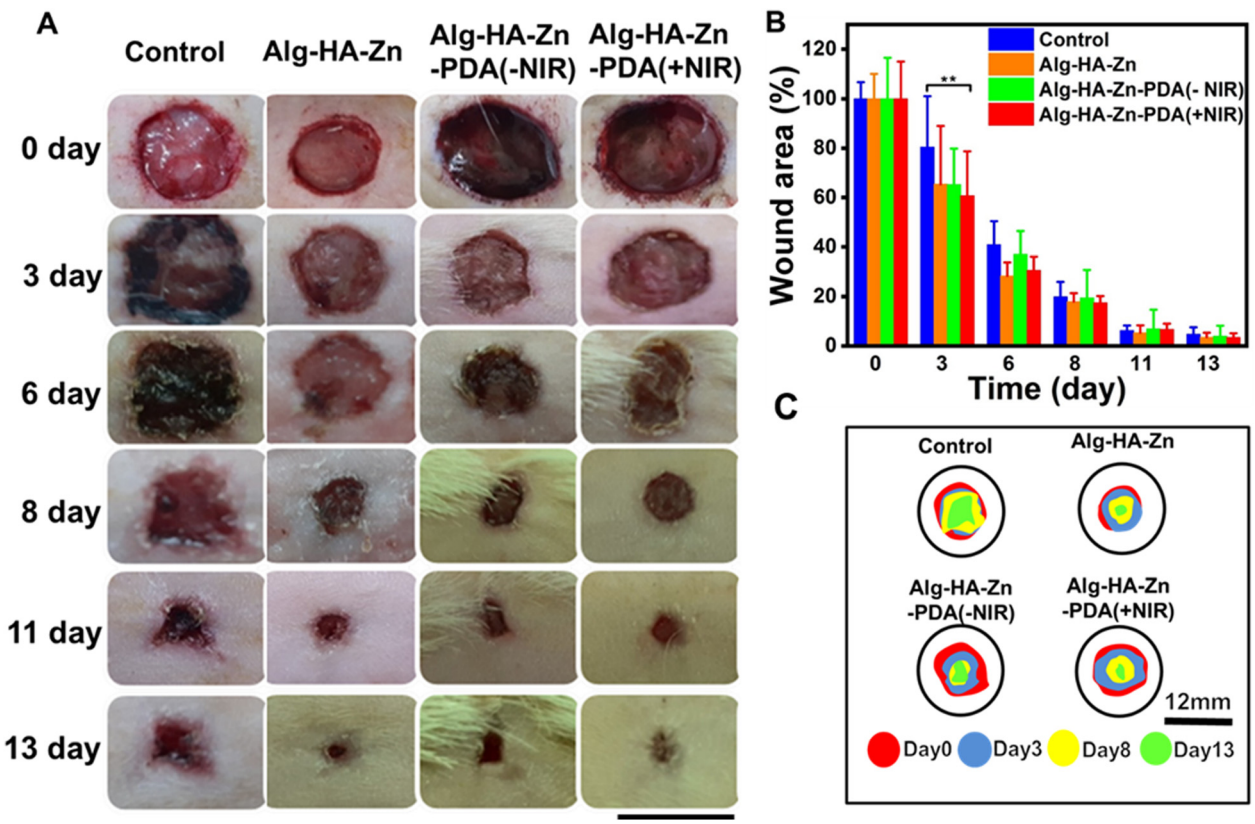

Fig. 10 *In vivo* assessment of Alg–HA–Zn–PDA hydrogel use to repair a full-thickness skin wound on the dorsal area of rats after treatment under laser irradiation. (A) Representative photographs of wound closure on days 0, 3, 6, 8, 11, and 13; scale bar: 12 mm. (B) The corresponding statistical diagram of wound area healing. (C) Schematic diagram of wound area during 13 days (mean ± SD, $n = 5$, **$p < 0.01$).

3.9. *In vivo* wound healing

A full-thickness infected wound model was created to evaluate the effects of the NIR-active hydrogels as wound dressings. All hydrogels accelerated skin repair compared to the control group by providing a suitable and moist microenvironment for the injury (Fig. 10A–C). The injectable hydrogels covered the shape of the irregular wound and filled the wound to prevent bacterial invasion while being able to absorb exudates.[93] The PDA-containing hydrogels resulted in faster healing than the Alg–HA–Zn hydrogel, which was due to the enhanced antioxidant and antibacterial properties of the NPs. Such healing was further enhanced by NIR irradiation, which had a great impact on the bacterial killing efficiency. In addition, Zn ions within the hydrogels had the potential to inhibit bacterial growth in the wound area, and they could promote wound healing *via* collagen synthesis and cellular growth.[40] After 14 days, the wounds treated with Alg–HA–Zn–PDA hydrogel were almost closed and even the wound site in some rats was covered by hair. Wound images at different time intervals were used to measure wound closure and quantitative wound areas (Fig. 10A and B). On day 3, the wound area in Alg–HA–Zn–PDA (+NIR) was 60.7%, much larger than that of the control (80.5%) ($p < 0.01$). Quantitatively, there was no significant different in wound closure after the 3rd day of the treatments. The healing process was also evaluated by hematoxylin and eosin (H&E)

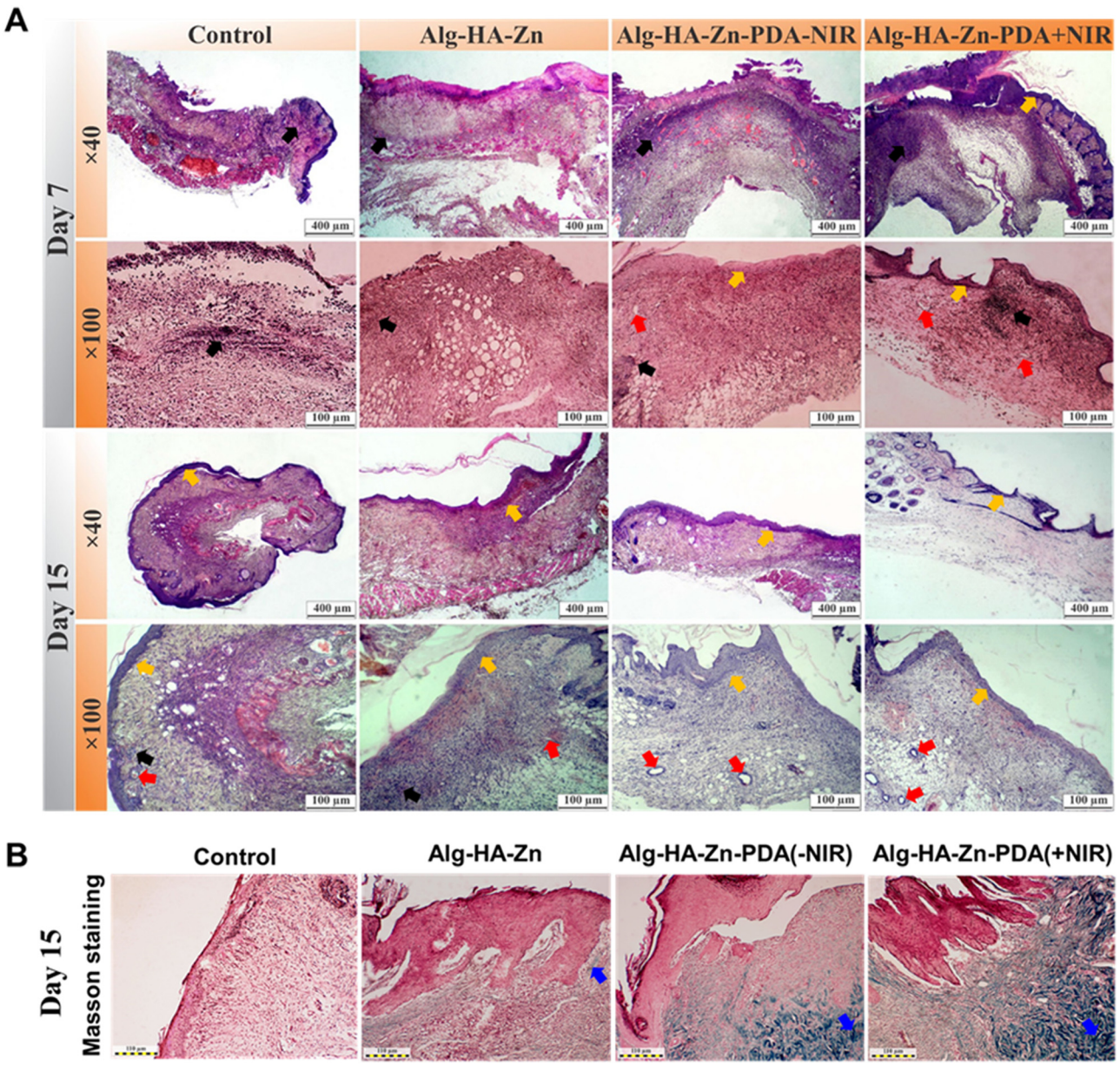

Fig. 11 *In vivo* histological analysis, (A) H&E staining of the wound section after 7 days and 15 days of treatment for all groups; scale bar: 100 μm. (B) Masson trichrome staining images of all groups after 15 days of treatment; scale bar: 110 μm. Black, yellow, red, and blue arrows show inflammatory cells, epidermis, blood vessels, and collagen fibers, respectively.

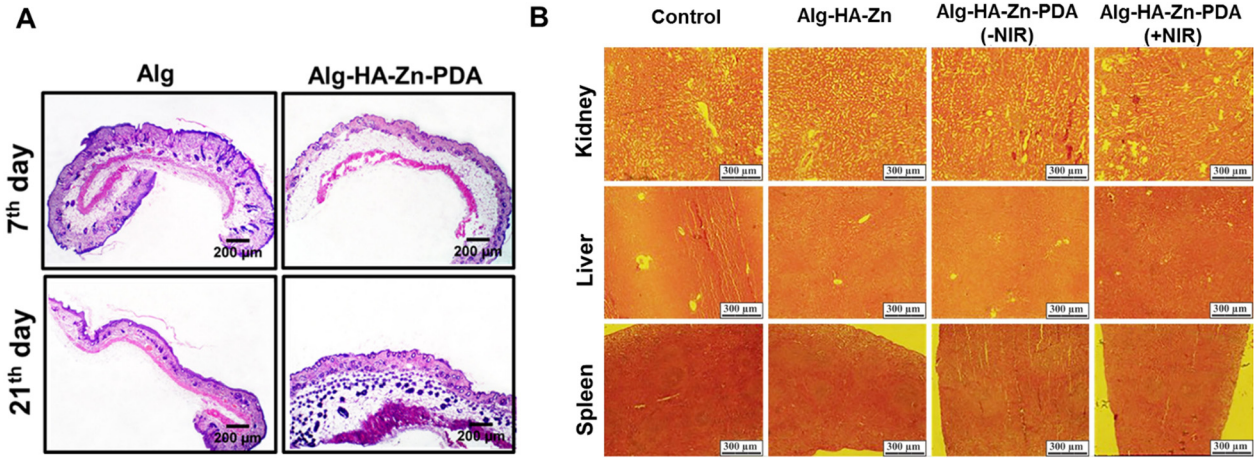

Fig. 12 *In vivo* toxicity evaluation. (A) The H&E staining images after subcutaneous injection of Alg and Alg–HA–Zn–PDA in rats and removed after 1 week and 3 weeks, scale bars: 200 μm. (B) H&E staining of the major organs (spleen, liver, and kidneys). Scale bar is 300 μm.

staining (Fig. 11A). At day 7, plenty of inflammatory cells (black arrows) were observed in all of the hydrogel groups. A layer of epithelium (yellow arrows) in group Alg–HA–Zn–PDA (+NIR) was formed while such a layer was not observed in other treated groups. On the 15th day, the Alg–HA–Zn–PDA (+NIR) and Alg–HA–Zn–PDA (−NIR) groups showed the basic structure of regenerated wound tissue including dermis and epithelium. Compared to the control and Alg–HA–Zn groups, the number of inflammatory cells was remarkably decreased in the Alg–HA–Zn–PDA groups. Importantly, the Alg–HA–Zn–PDA (+NIR) group exhibited a thickened epidermis and increased blood vessels (red arrows), revealing that the group possesses the best wound healing performance (Fig. 11A). Masson's trichrome staining was performed to analyze collagen deposition (blue arrows) (Fig. 11B). Larger amounts of collagen deposition were observed in the Alg–HA–Zn–PDA (+NIR) group. In addition, the extent of collagen in the Alg–HA–Zn–PDA–NIR group was lower than that of Alg–HA–Zn and the control groups, indicating that PDA increased collagen formation.[75] These results of H&E and Masson staining showed that the NIR-responsive HA–Zn–PDA hydrogel could accelerate the infected wound healing process by improving epidermis formation, boosting dermal tissue generation, and increasing collagen deposition.

3.10. *In vivo* toxicity evaluation

The *in vivo* acute inflammatory response of the Alg and Alg–HA–Zn–PDA was evaluated by H&E staining after 7 and 21 days of subcutaneous implantation.[94] Alg, as a biocompatible polymer, was used as the control group. After subcutaneous injection of the samples, the epidermis, dermis, and hypodermis were monitored on both days 7 and 21. Compared with the Alg group, many thick hair follicles were observed in the Alg–HA–Zn–PDA group and the regenerated skin was almost similar to natural skin. This finding can be attributed to the presence of zinc in the hydrogel. Altogether, our *in vivo* studies using H&E staining revealed high biocompatibility of the Alg–HA–Zn–PDA hydrogel (Fig. 12A). The histological analysis of the major rat organs (kidney, liver, and spleen) was also investigated (Fig. 12B). The H&E staining images of different organ slices demonstrated that none of the groups induce significant organ abnormalities or damage, indicating the excellent *in vivo* biosafety of the hydrogels.

4. Conclusion

In conclusion, we successfully developed a multifunctional injectable NIR-responsive hydrogel for infected wound healing. The hydrogel was fabricated by HA, Alg, and PDA through the metal coordination effect of Zn^{2+} as the crosslinker. The PDA could provide excellent photothermal and antioxidant activity to the hybrid hydrogel. In addition, the Zn^{2+} released from the hydrogel not only endowed the hydrogel with high antibacterial properties but also regulated cell behavior to promote the proliferation of fibroblasts. Our results revealed that the antibacterial performance of the photoactive hydrogel increased when a NIR laser was used. Furthermore, the injectable hydrogel could perfectly fill the shape of irregular wounds to provide an appropriate environment for cell growth. Our findings showed that the Alg–HA–Zn–PDA hydrogel exhibited better skin tissue regeneration than the Alg–HA–Zn hydrogel in terms of wound closure rate, collagen deposition, hair follicles, epidermis, and vessel blood regeneration, demonstrating that the incorporation of PDA improved the wound healing effect of the hydrogel. Importantly, when NIR light (808 nm) was used in the treatment, the healing effect was enhanced further, indicating the essential role of hyperthermia in the wound-healing process. The hydrogel was biocompatible and showed good hemostatic performance. With all the above-mentioned promising properties, the NIR-active Alg–HA–Zn–PDA hydrogel with high antibacterial, antioxidant, and healing properties can be considered a highly efficient dressing material for wound healing applications.

Conflicts of interest

There are no conflicts to declare.

Acknowledgements

This work was supported by the Zanjan University of Medical Sciences (No. A-12-1143-1) and it was also supported by the National Animal Modeling Network and *In vivo* Research, Council for Development of Stem Cell Sciences and Technologies, Vice-Presidency for Science and Technology (grant number 98/11612).

References

1 P. P. Kalelkar, M. Riddick and A. J. García, *Nat. Rev. Mater.*, 2022, **7**, 39–54.
2 Y. Golan, *Clin. Infect. Dis.*, 2019, **68**, S206–S212.
3 A. Maleki, J. He, S. Bochani, V. Nosrati, M.-A. Shahbazi and B. Guo, *ACS Nano*, 2021, **15**, 18895–18930.
4 Y. Sang, W. Li, H. Liu, L. Zhang, H. Wang, Z. Liu, J. Ren and X. Qu, *Adv. Funct. Mater.*, 2019, **29**, 1900518.
5 Y. Yang, M. Li, G. Pan, J. Chen and B. Guo, *Adv. Funct. Mater.*, 2023, 2214089.
6 V. Alinezhad, K. Esmaeilzadeh, H. Bagheri, H. Zeighami, A. Kalantari-Hesari, R. Jafari, P. Makvandi, Y. Xu, H. Mohammadi and M.-A. Shahbazi, *Biomater. Sci.*, 2023, **11**, 5872–5892.
7 S. Bochani, A. Zarepour, A. Kalantari-Hesari, F. Haghi, M.-A. Shahbazi, A. Zarrabi, S. Taheri and A. Maleki, *J. Mater. Chem. B*, 2023, **11**, 8056–8068.
8 W. Zhang, Z. Yang, M. Zhang, J. He, S. Li, X. Sun and P. Ni, *J. Mater. Chem. B*, 2023, **11**, 4922–4933.
9 Y.-W. Ding, Z.-Y. Wang, Z.-W. Ren, X.-W. Zhang and D.-X. Wei, *Biomater. Sci.*, 2022, **10**, 3393–3409.
10 J. Qu, X. Zhao, Y. Liang, Y. Xu, P. X. Ma and B. Guo, *Chem. Eng. J.*, 2019, **362**, 548–560.
11 X. Wang, K. Su, L. Tan, X. Liu, Z. Cui, D. Jing, X. Yang, Y. Liang, Z. Li and S. Zhu, *ACS Appl. Mater. Interfaces*, 2019, **11**, 15014–15027.
12 Y. Zhang, Y. Zheng, F. Shu, R. Zhou, B. Bao, S. Xiao, K. Li, Q. Lin, L. Zhu and Z. Xia, *Carbohydr. Polym.*, 2022, **276**, 118752.
13 M. Abazari, T. Akbari, M. Hasani, E. Sharifikolouei, M. Raoufi, A. Foroumadi, M. Sharifzadeh, L. Firoozpour and M. Khoobi, *Carbohydr. Polym.*, 2022, **294**, 119808.
14 J. Qin, M. Li, M. Yuan, X. Shi, J. Song, Y. He, H. Mao, D. Kong and Z. Gu, *ACS Appl. Mater. Interfaces*, 2022, **14**, 22426–22442.
15 L. Zhang, M. Liu, Y. Zhang and R. Pei, *Biomacromolecules*, 2020, **21**, 3966–3983.
16 W. Peng, D. Li, K. Dai, Y. Wang, P. Song, H. Li, P. Tang, Z. Zhang, Z. Li and Y. Zhou, *Int. J. Biol. Macromol.*, 2022, **208**, 400–408.
17 H. Huang, H. Chen, X. Wang, F. Qiu, H. Liu, J. Lu, L. Tong, Y. Yang, X. Wang and H. Wu, *ACS Biomater. Sci. Eng.*, 2019, **5**, 5498–5505.
18 Y. Jia, X. Zhang, W. Yang, C. Lin, B. Tao, Z. Deng, P. Gao, Y. Yang and K. Cai, *J. Mater. Chem. B*, 2022, **10**, 2875–2888.
19 L. Liang, T. Liu, Q. Ouyang, S. Li and C. Li, *Carbohydr. Polym.*, 2022, **295**, 119843.
20 Y. Cao, H. Cong, B. Yu and Y. Shen, *J. Mater. Chem. B*, 2023, **11**, 2801–2829.
21 Y. Wang, Y. Shi, J. Liu, W. Yang, H. Tang and H. Li, *Int. J. Pharm.*, 2023, **642**, 123140.
22 G. Mao, S. Tian, Y. Shi, J. Yang, H. Li, H. Tang and W. Yang, *Carbohydr. Polym.*, 2023, **311**, 120757.
23 J. Jiang, X. Li, H. Li, X. Lv, Y. Xu, Y. Hu, Y. Song, J. Shao, S. Li and D. Yang, *J. Mater. Chem. B*, 2023, **11**, 6746–6761.
24 N. R. Barros, Y. Chen, V. Hosseini, W. Wang, R. Nasiri, M. Mahmoodi, E. P. Yalcintas, R. Haghniaz, M. M. Mecwan and S. Karamikamkar, *Biomater. Sci.*, 2021, **9**, 6653–6672.
25 G. Gao, Y.-W. Jiang, H.-R. Jia and F.-G. Wu, *Biomaterials*, 2019, **188**, 83–95.
26 H. Liu, X. Zhu, H. Guo, H. Huang, S. Huang, S. Huang, W. Xue, P. Zhu and R. Guo, *Appl. Mater. Today*, 2020, **20**, 100781.
27 L. Han, X. Lu, K. Liu, K. Wang, L. Fang, L.-T. Weng, H. Zhang, Y. Tang, F. Ren and C. Zhao, *ACS Nano*, 2017, **11**, 2561–2574.
28 Y. Liang, X. Zhao, T. Hu, B. Chen, Z. Yin, P. X. Ma and B. Guo, *Small*, 2019, **15**, 1900046.
29 W. Liao, D. Yang, Z. Xu, L. Zhao, C. Mu, D. Li and L. Ge, *Adv. Healthcare Mater.*, 2023, 2203054.
30 W. Wang, H. Sheng, D. Cao, F. Zhang, W. Zhang, F. Yan, D. Ding and N. Cheng, *Int. J. Biol. Macromol.*, 2022, **200**, 77–86.
31 P. Zhao, Y. Zhang, X. Chen, C. Xu, J. Guo, M. Deng, X. Qu, P. Huang, Z. Feng and J. Zhang, *Adv. Sci.*, 2023, 2206585.
32 Z. Song, Y. Wen, F. Teng, M. Wang, N. Liu and R. Feng, *New J. Chem.*, 2022, **46**, 3674–3686.
33 J. Pan, Y. Jin, S. Lai, L. Shi, W. Fan and Y. Shen, *Chem. Eng. J.*, 2019, **370**, 1228–1238.
34 H. Chen, C. Peng, L. Wang, X. Li, M. Yang, H. Liu, H. Qin and W. Chen, *Chem. Eng. J.*, 2021, **403**, 126341.
35 N. Ninan, A. Forget, V. P. Shastri, N. H. Voelcker and A. Blencowe, *ACS Appl. Mater. Interfaces*, 2016, **8**, 28511–28521.
36 Y. Li, R. Fu, Z. Duan, C. Zhu and D. Fan, *Bioact. Mater.*, 2022, **9**, 461–474.
37 R. Yang, M. Hou, Y. Gao, L. Zhang, Z. Xu, Y. Kang and P. Xue, *Nanoscale*, 2019, **11**, 5717–5731.
38 B. Guo, Y. Liang and R. Dong, *Nat. Protoc.*, 2023, **18**, 3322–3354.
39 P. Stenberg and B. Roth, *Med. Hypotheses*, 2015, **84**, 331–335.
40 G. Rath, T. Hussain, G. Chauhan, T. Garg and A. K. Goyal, *Mater. Sci. Eng., C*, 2016, **58**, 242–253.
41 Y. Xiang, C. Mao, X. Liu, Z. Cui, D. Jing, X. Yang, Y. Liang, Z. Li, S. Zhu and Y. Zheng, *Small*, 2019, **15**, 1900322.
42 Y. Gan, C. Lin, H. Zhu, X. Cheng, C. Liu and J. Shi, *New J. Chem.*, 2022, **46**, 8043–8052.
43 J. Prakash, K. Venkataprasanna and G. D. Venkatasubbu, *New J. Chem.*, 2022, **46**, 13325–13344.
44 X. Zhang, Y. Tang, P. Wang, Y. Wang, T. Wu, T. Li, S. Huang, J. Zhang, H. Wang and S. Ma, *New J. Chem.*, 2022, **46**, 13838–13855.

45 Y. Liu, K. Ai, J. Liu, M. Deng, Y. He and L. Lu, *Adv. Mater.*, 2013, **25**, 1353–1359.
46 L. Wang, X. Zhang, K. Yang, Y. V. Fu, T. Xu, S. Li, D. Zhang, L. N. Wang and C. S. Lee, *Adv. Funct. Mater.*, 2020, **30**, 1904156.
47 J. Qu, X. Zhao, P. X. Ma and B. Guo, *Acta Biomater.*, 2017, **58**, 168–180.
48 Y. Li, X. Liu, L. Tan, Z. Cui, X. Yang, Y. Zheng, K. W. K. Yeung, P. K. Chu and S. Wu, *Adv. Funct. Mater.*, 2018, **28**, 1800299.
49 K. Musaie, S. Abbaszadeh, V. Nosrati-Siahmazgi, M. Qahremani, S. Wang, M. R. Eskandari, S. V. Niknezhad, F. Haghi, Y. Li and B. Xiao, *Biomater. Sci.*, 2023, **11**, 2486–2503.
50 B. Tao, C. Lin, Z. Yuan, Y. He, M. Chen, K. Li, J. Hu, Y. Yang, Z. Xia and K. Cai, *Chem. Eng. J.*, 2021, **403**, 126182.
51 M.-A. Shahbazi, M. Hamidi, E. M. Mäkilä, H. Zhang, P. V. Almeida, M. Kaasalainen, J. J. Salonen, J. T. Hirvonen and H. A. Santos, *Biomaterials*, 2013, **34**, 7776–7789.
52 S. Wei, P. Xu, Z. Yao, X. Cui, X. Lei, L. Li, Y. Dong, W. Zhu, R. Guo and B. Cheng, *Acta Biomater.*, 2021, **124**, 205–218.
53 B. Tao, C. Lin, Y. Deng, Z. Yuan, X. Shen, M. Chen, Y. He, Z. Peng, Y. Hu and K. Cai, *J. Mater. Chem. B*, 2019, **7**, 2534–2548.
54 M. C. Straccia, G. G. d'Ayala, I. Romano and P. Laurienzo, *Carbohydr. Polym.*, 2015, **125**, 103–112.
55 J. Amirian, T. T. T. Van, S.-H. Bae, H.-I. Jung, H.-J. Choi, H.-D. Cho and B.-T. Lee, *Int. J. Biol. Macromol.*, 2017, **105**, 143–153.
56 N. Pandey, A. Hakamivala, C. Xu, P. Hariharan, B. Radionov, Z. Huang, J. Liao, L. Tang, P. Zimmern and K. T. Nguyen, *Adv. Healthcare Mater.*, 2018, **7**, 1701069.
57 S. K. Papageorgiou, E. P. Kouvelos, E. P. Favvas, A. A. Sapalidis, G. E. Romanos and F. K. Katsaros, *Carbohydr. Res.*, 2010, **345**, 469–473.
58 R. Batul, M. Bhave, P. J. Mahon and A. Yu, *Molecules*, 2020, **25**, 2090.
59 X. Liu, J. Cao, H. Li, J. Li, Q. Jin, K. Ren and J. Ji, *ACS Nano*, 2013, **7**, 9384–9395.
60 H. Luo, C. Gu, W. Zheng, F. Dai, X. Wang and Z. Zheng, *RSC Adv.*, 2015, **5**, 13470–13477.
61 Y. Liu, L. J. Duan, M. J. Kim, J.-H. Kim and D. J. Chung, *Macromol. Res.*, 2014, **22**, 240–247.
62 S. Bochani, A. Kalantari-Hesari, F. Haghi, V. Alinezhad, H. Bagheri, P. Makvandi, M.-A. Shahbazi, A. Salimi, I. Hirata and V. Mattoli, *ACS Appl. Bio Mater.*, 2022, **5**, 4435–4453.
63 A. Serafin, M. Culebras and M. N. Collins, *Int. J. Biol. Macromol.*, 2023, **233**, 123438.
64 G. Wang, X. Wang and L. Huang, *Biotechnol. Biotechnol. Equip.*, 2017, **31**, 766–773.
65 T. Su, L. Wu, G. Zuo, X. Pan, M. Shi, C. Zhang, X. Qi and W. Dong, *Environ. Res.*, 2020, **182**, 109010.
66 B. Singh, S. Sharma and A. Dhiman, *Int. J. Pharm.*, 2013, **457**, 82–91.
67 H. Huang, R. Chen, S. Yang, L. Li, Y. Liu and J. Huang, *High Perform. Polym.*, 2020, **32**, 286–295.
68 X. Qi, W. Pan, X. Tong, T. Gao, Y. Xiang, S. You, R. Mao, J. Chi, R. Hu and W. Zhang, *Carbohydr. Polym.*, 2021, **264**, 118046.
69 G. Flores-Carrasco, J. Carrillo-López, J. Luna-López, R. Martínez-Martínez, N. Espinosa-Torres and M. Rabanal, *Adv. Mater. Sci. Eng.*, 2014, **2014**, 780206.
70 D. G. Miranda, S. M. Malmonge, D. M. Campos, N. G. Attik, B. Grosgogeat and K. Gritsch, *J. Biomed. Mater. Res., Part B*, 2016, **104**, 1691–1702.
71 T. Li, X. Liu, L. Li, Y. Wang, P. Ma, M. Chen and W. Dong, *J. Polym. Res.*, 2019, **26**, 1–12.
72 A. Salisu, M. M. Sanagi, A. Abu Naim, K. J. Abd Karim, W. A. Wan Ibrahim and U. Abdulganiyu, *Polym. Bull.*, 2016, **73**, 519–537.
73 E. Goh, X. Xu and P. McCormick, *Scr. Mater.*, 2014, **78**, 49–52.
74 Q. Zeng, Y. Qian, Y. Huang, F. Ding, X. Qi and J. Shen, *Bioact. Mater.*, 2021, **6**, 2647–2657.
75 Y. Li, R. Fu, Z. Duan, C. Zhu and D. Fan, *ACS Nano*, 2022, **16**, 7486–7502.
76 X. Zhao, Y. Liang, Y. Huang, J. He, Y. Han and B. Guo, *Adv. Funct. Mater.*, 2020, **30**, 1910748.
77 H. Huang and C. Sorensen, *Phys. Rev. E: Stat. Phys., Plasmas, Fluids, Relat. Interdiscip. Top.*, 1996, **53**, 5075.
78 S. Wang, H. Zheng, L. Zhou, F. Cheng, Z. Liu, H. Zhang and Q. Zhang, *Biomaterials*, 2020, **260**, 120314.
79 M. Fronza, B. Heinzmann, M. Hamburger, S. Laufer and I. Merfort, *J. Ethnopharmacol.*, 2009, **126**, 463–467.
80 C. W. Hsiao, H. L. Chen, Z. X. Liao, R. Sureshbabu, H. C. Hsiao, S. J. Lin, Y. Chang and H. W. Sung, *Adv. Funct. Mater.*, 2015, **25**, 721–728.
81 M.-C. Wu, A. R. Deokar, J.-H. Liao, P.-Y. Shih and Y.-C. Ling, *ACS Nano*, 2013, **7**, 1281–1290.
82 H.-S. Joo and M. Otto, *Chem. Biol.*, 2012, **19**, 1503–1513.
83 H. Zhu, X. Cheng, J. Zhang, Q. Wu, C. Liu and J. Shi, *J. Mater. Chem. B*, 2023, **11**, 618–630.
84 V. Kant, A. Gopal, N. N. Pathak, P. Kumar, S. K. Tandan and D. Kumar, *Int. Immunopharmacol.*, 2014, **20**, 322–330.
85 H. Sies, C. Berndt and D. Jones, *Annu. Rev. Biochem.*, 2017, **20**, 715–748.
86 W. Chen, X. Shen, Y. Hu, K. Xu, Q. Ran, Y. Yu, L. Dai, Z. Yuan, L. Huang and T. Shen, *Biomaterials*, 2017, **114**, 82–96.
87 S. Hong, K. Yang, B. Kang, C. Lee, I. T. Song, E. Byun, K. I. Park, S. W. Cho and H. Lee, *Adv. Funct. Mater.*, 2013, **23**, 1774–1780.
88 Y. Liang, X. Zhao, T. Hu, Y. Han and B. Guo, *J. Colloid Interface Sci.*, 2019, **556**, 514–528.
89 X. Zhao, B. Guo, H. Wu, Y. Liang and P. X. Ma, *Nat. Commun.*, 2018, **9**, 2784.
90 J. Chen, X. Li, L. Li, T. Zhang, Q. Zhang, F. Wu, D. Wang, H. Hu, C. Tian and D. Liao, *Cell Res.*, 2019, **29**, 711–724.
91 J. Ren, X. Yin, Y. Chen, H. Su, K. Wang, L. Zhang, J. Zhu and C. Zhang, *Biomaterials*, 2020, **249**, 120019.
92 S. Tubek, P. Grzanka and I. Tubek, *Biol. Trace Elem. Res.*, 2008, **121**, 1–8.
93 S. Wang, H. Zheng, L. Zhou, F. Cheng, Z. Liu, H. Zhang, L. Wang and Q. Zhang, *Nano Lett.*, 2020, **20**, 5149–5158.
94 Y. Liang, Z. Li, Y. Huang, R. Yu and B. Guo, *ACS Nano*, 2021, **15**, 7078–7093.

